JGR Atmospheres

RESEARCH ARTICLE
10.1029/2018JD029720

Key Points:
- The CAM and CAM/CARMA models failed to produce observed tropical tropopause layer cloud features over the western Pacific Ocean
- TTL cirrus have large horizontal scale but low ice water content and need different macrophysics to be properly represented in CAM/CARMA
- Corrections to cloud fraction, cold point temperature, and the inclusion of a simple gravity wave scheme improve simulations of TTL cirrus

Correspondence to:
C. Maloney,
christopher.maloney@colorado.edu

Citation:
Maloney, C., Bardeen, C., Toon, O. B., Jensen, E., Woods, S., Thornberry, T., et al. (2019). An evaluation of the representation of tropical tropopause cirrus in the CESM/CARMA model using satellite and aircraft observations. *Journal of Geophysical Research: Atmospheres*, *124*, 8659–8687. https://doi.org/10.1029/2018JD029720

Received 24 SEP 2018
Accepted 9 JUL 2019
Accepted article online 14 JUL 2019
Published online 4 AUG 2019

An Evaluation of the Representation of Tropical Tropopause Cirrus in the CESM/CARMA Model Using Satellite and Aircraft Observations

Christopher Maloney[1,2], Charles Bardeen[3], Owen Brian Toon[1,2], Eric Jensen[4], Sarah Woods[5], Troy Thornberry[6], Leonhard Pfister[4], Glenn Diskin[7], and Thao Paul Bui[4]

[1]Department of Atmospheric and Oceanic Sciences, University of Colorado Boulder, Boulder, CO, USA, [2]Laboratory for Atmospheric and Space Physics, University of Colorado Boulder, Boulder, CO, USA, [3]National Center for Atmospheric Research, Boulder, CO, USA, [4]NASA Ames Research Center, Mountain View, CA, USA, [5]Spec Inc., Boulder, CO, USA, [6]NOAA/Earth System Research Laboratory and Cooperative Institute for Research in Environmental Sciences, Boulder, CO, USA, [7]NASA Langley Research Center, Hampton, VA, USA

Abstract Observations from the third campaign of the National Aeronautics and Space Administration Airborne Tropical Tropopause Experiment (ATTREX 3) field mission and Cloud-Aerosol Lidar and Infrared Pathfinder Satellite Observations satellite mission are used to evaluate simulations of tropical tropopause layer (TTL) cirrus clouds in the Community Earth System Model's (CESM) Community Atmosphere Model, CAM5. In this study, CAM5 is coupled with a sectional ice cloud model, the Community Aerosol and Radiation Model for Atmospheres (CARMA). We find that both model variants underrepresent cloud frequency along the ATTREX 3 flight path and both poorly represent relative humidity in the TTL. Furthermore, simulated in-cloud ice size distributions contained erroneous amounts of ice crystals throughout the distribution. In response, we present a modified ice cloud fraction scheme that boosts the cloud fraction within the TTL. Due to coarse vertical model resolution in the TTL, we also prescribe a 2-K decrease in cold point tropopause temperatures to better align with observed temperatures. Our modifications improve both CAM5 and CAM5/CARMA's in-cloud ice size and mass distributions. However, only CAM5/CARMA has a significant improvement in cloud frequency and relative humidity. An investigation of cloud extinction in the ATTREX 3 region found that each model variant struggles to reproduce observed extinctions. As a first-order approximation, we introduce randomly generated temperature perturbations to simulate the effect of gravity waves into the CAM5/CARMA simulation. These gravity waves significantly increase the incidence of low extinction (<0.02 km^{-1}) values, ice cloud fraction between 16 and 18 km, and ice crystal smaller than 100-μm concentrations but provided only small changes to high extinction values.

Plain Language Summary We use observations from aircraft and satellite missions to evaluate the representation of upper tropical tropospheric ice clouds in a widely used global climate model. The goal of this study is to produce a more realistic representation of ice clouds within a climatologically influential region. Such model improvements will help us better predict future climates. We find that the model used in this study fails to properly represent the ice clouds along the aircraft flight path and is too dry. In response, we introduce modifications that boost the cloud coverage in the upper troposphere. Our modifications improve the frequency of clouds along the aircraft flight path, as well as the simulated number and mass of ice crystals inside ice clouds. The modifications also moisten the model. We also find that simulations are unable to reproduce proper cloud extinctions. As a first step to address this problem, we introduce a set of randomly generated temperature fluctuations into the simulated upper troposphere. These temperature fluctuations improve instances of transparent clouds, but they fail to improve the amount of high extinction clouds. Future work should focus on better temperature fluctuation parameterizations and better cloud parameterizations to address these model shortcomings.

1. Introduction

Cirrus clouds cover approximately 20–25% of Earth's surface at any given time (Rossow & Schiffer, 1999; Wang et al., 1994). As a result, cirrus clouds play an important role in Earth's climate. They dehydrate air as it enters the stratosphere (Jensen et al., 1996, 2010), strongly impact the radiation budget (Comstock et al., 2002; Yang et al., 2010), and through cloud heating potentially influence the tropical troposphere-stratosphere exchange (Corti et al., 2006). In order to improve the understanding of cirrus clouds, numerous studies ranging from laboratory experiments focused on ice nucleation (e.g., Hoose & Möhler, 2012), to field measurements of cirrus (e.g., Davis et al., 2010; Lawson et al., 2008; Woods et al., 2018), to satellite missions (e.g., Wang & Dessler, 2012; Winker et al., 2009) have been undertaken.

Due to the role cirrus clouds play in climate, it is important that general circulation models (GCMs) properly represent these clouds. However, the representation of ice clouds in GCMs varies greatly, resulting in a wide range of simulated ice water contents (IWCs; Jiang et al., 2012; Waliser et al., 2009). Furthermore, the horizontal resolution of GCMs is often too coarse to capture the small spatial and temporal scale of convectively generated cirrus clouds (Pfister et al., 2001). Conversely, in situ formed cirrus in the tropical tropopause layer (TTL) often have a horizontal extent comparable to typical GCM horizontal resolutions but frequently have a finer vertical extent (Massie et al., 2010; Pfister et al., 2001).

A previous study by Bardeen et al. (2013) shows that using a sized-resolved treatment of cloud ice number and mass developed from the Community Aerosol and Radiation Model for Atmospheres (CARMA, Bardeen et al., 2008; Toon et al., 1988; Turco et al., 1979), coupled with the National Science Foundation/Department of Energy Community Atmosphere Model (CAM), improves the global distribution of cirrus cloud fraction, IWC, and ice water path relative to the default two-moment cloud schemes used by Morrison and Gettelman (2008) in CAM. These results were obtained by comparing simulations to the dual lidar-radar DARDAR (Delanoë & Hogan, 2008; Delanoë & Hogan, 2010) and 2C-ICE (Deng et al., 2010) data sets. This study builds upon previous work by narrowing the focus from cirrus globally to TTL cirrus, which is an area where CAM simulations still struggle (Bardeen et al., 2013).

In the tropics (20°N to 20°S) TTL cirrus clouds can cover 30% of the total area (Haladay & Stephens, 2009), with the location of maximum cloud occurrence shifting north and south of the equator following seasonal shifts of the Intertropical Convergence Zone (ITCZ; Yang et al., 2010). The TTL serves as the interface between the upper troposphere and lower stratosphere (UT/LS). The TTL lies just above the mean level of convective outflow (~14 km) and below 18.5 km (Fueglistaler et al., 2009). Air ascends through the TTL where the formation of cirrus and sedimentation of ice particles dehydrates the air (e.g., Fueglistaler et al., 2009; Randel & Jensen, 2013). Within the TTL cirrus clouds exist in two forms: (1) a high (cloud base above 15 km), optically thin ($\tau < 0.1$), laminar cloud layer; and (2) a lower cloud layer with more structure which is more optically thick (e.g., Comstock et al., 2002; Pfister et al., 2001).

While satellite observations of TTL cirrus are bountiful, the high altitude and remote nature of these clouds make in situ observations difficult to obtain (Fueglistaler et al., 2009) and therefore sparse. Further complicating matters is that even highly sensitive satellite instruments can struggle to capture the most optically thin cirrus in the TTL, such as subvisible cirrus ($\tau < 0.03$; Sassen & Cho, 1992). For example, Davis et al. (2010) showed that the lidar onboard the Cloud-Aerosol Lidar and Infrared Pathfinder Satellite Observations (CALIPSO) satellite misses approximately two thirds of the subvisible cirrus with $\tau < 0.01$ compared to the Cloud Physics Lidar (CPL) aircraft-borne instrument. Such limitations to observations of TTL cirrus have resulted in difficulty fully understanding these clouds, especially in the tropical western Pacific (TWP) where there are very limited aircraft observations. This lack of data is problematic because the TWP is known to play an important climatological role as it acts as a source for air entering the LS during boreal winter (Bergman et al., 2012).

The third deployment of National Aeronautics and Space Administration (NASA)'s Airborne Tropical Tropopause Experiment (ATTREX 3; Jensen et al., 2016), which occurred between January and March 2014, addressed both issues of limited in situ cirrus observations and limited observations over the TWP. ATTREX 3, which operated out of Andersen Air Force Base in Guam, captured 34 hr of in situ TTL cirrus observations over the course of the mission.

The focus of the present study is to utilize in situ observations from the ATTREX 3 campaign alongside satellite observations, primarily from CALIPSO mission, to assess the TTL cirrus cloud representation in version 5 of CAM (CAM5). TTL cirrus representations in both the standard CAM5 model and CAM5 coupled with CARMA are assessed here. Due to the optically thin nature of TTL cirrus, it is necessary to utilize the sensitive CALIPSO lidar Level 2 product for model evaluation. Recently, the CALIPSO version 4 data set has been released, which addresses a classification error that caused optically thin, TTL cirrus clouds to be erroneously identified as aerosol layers (Getzewich et al., 2016). The updated data are used in this study. We further present a modification to the treatment of TTL ice clouds which require different assumptions due to their expansive horizontal extent and low IWC.

In section 2, both the ATTREX 3 and CALIPSO missions are described, as well as the model variants used in this study. Comparisons of simulations with observations can be found in section 3, while section 4 provides a discussion of results. Section 5 summarizes the information obtained from this study.

2. Methods

2.1. ATTREX 3 Overview

The NASA ATTREX (Jensen, Pfister, et al., 2016) was a 5-year mission tasked with observing TTL cirrus over the tropical Pacific Ocean. The mission had three main science goals: to investigate the role of stratospheric water vapor in Earth's climate, to investigate the dehydration of tropospheric air entering the stratosphere, and to investigate the chemical composition and the physical processes that occur in the TTL. The third campaign of the mission was flown from Andersen Air Force Base in Guam and mainly took place over the western Pacific Ocean. Previous ATTREX campaigns occurred over the eastern Pacific Ocean. The mission used a NASA Global Hawk aircraft to collect in situ and remote sensing observations of the TTL. The aircraft was chosen for the ATTREX missions due to its high altitude and long flight duration capabilities. The Global Hawk is capable of flight times upward of 22 hr with a true airspeed of ~170 m/s at cruise altitudes of 14 to almost 19 km. This capability allowed for observations in the UT/LS over much of the TWP region over the course of about 6 weeks. The following subsections describe the various instruments on board the Global Hawk whose data are used in this study.

2.1.1. ATTREX 3 Measurement Techniques

The ATTREX measurements included in this study were made using several different instruments. The SPEC Inc. Hawkeye probe is a combination of three instruments that measure particles between 1 μm and 4 mm in diameter: the 2D-Stereo Optical Array Probe (2D-S, Lawson et al., 2006), the Cloud Particle Imager (Lawson et al., 2001), and the Fast Cloud Droplet Probe (FCDP, Lawson et al., 2017). This study uses ice crystal number concentrations and mass from the Hawkeye 2D-S (H-2DS hereafter) and FCDP (H-FCDP hereafter) instruments, as well as an additional set of ice crystal concentration observations from a standalone FCDP (S-FCDP hereafter) also onboard the Global Hawk. Optical extinction estimates calculated from the H-2DS measurement of particle area are also used in the analysis. Additional details of the Hawkeye data collection, treatment, and observed microphysics may be found in Woods et al. (2018). Water vapor measurements for this study are from the NASA diode laser hygrometer (DLH, Diskin et al., 2002) and the National Oceanic and Atmospheric Administration Water (NW, Thornberry et al., 2015) instruments. The excellent agreement between the water vapor values reported by the DLH and NW instruments over the course of the ATTREX mission provides confidence in the accuracy of the measurements even at low mixing ratios (Jensen, Pfister, et al., 2016). Lastly, nadir facing lidar observations of 532-nm backscatter are provided by the NASA Goddard Space Flight Center CPL. CPL measures backscattered light at three wavelengths, 335, 532, and 1,064 nm (McGill et al., 2002). It should be noted that CPL was inoperable for the final two flights of ATTREX 3 due to equipment failure. Due to Global Hawk specific operational constraints, CPL was only active at cruise altitudes and shut off during descents, limiting in-cloud observations.

2.2. The CALIPSO Satellite

This study uses two sets of observations obtained from the Cloud-Aerosol Lidar with Orthogonal Polarization (CALIOP) onboard the CALIPSO satellite (Winker et al., 2003). Measurements of extinction from the CALIOP Level 2 cloud profile version 4 (CAL-LV2 hereafter; Winker et al., 2006) are used to evaluate finer-scale cloud features within the ATTREX 3 region. The CAL-LV2 data provide a high-resolution vertical profile that can be used alongside the various cloud probes onboard the Global Hawk to evaluate model simulations. For this evaluation, observations of liquid and mixed phase clouds are excluded as this study's focus is upon TTL ice clouds. CALIOP has an observable backscatter limit of ~0.001 sr^{-1} that corresponds with a minimum observable extinction limit of 2×10^{-4} km^{-1} (Avery et al., 2012; Winker et al., 2007; Winker et al., 2010).

The second CALIPSO data set used in this study to evaluate large-scale cloud features is the $1 \times 1°$ CALIPSO-GOCCP data set (Chepfer et al., 2010). CALIPSO-GOCCP was created with the purpose of providing a set of global CALIPSO observations that diagnose cloud properties in the same manner as the Cloud Feedback Model Intercomparison Project (CFMIP) Observation Simulator Package (COSP) in CAM. The strength of the CALIPSO-GOCCP data set is that it ensures the differences between model simulations and satellite observations reveal biases between model and observations instead of differences between the definition of clouds or diagnostics (Chepfer et al., 2010).

2.3. Model Overview

As previously mentioned, the goal of this work is to evaluate the CAM5/MG and CAM5/CARMA models' performance in simulating TTL cirrus clouds along the ATTREX 3 flight track. The following three subsections briefly describe the default CAM5 microphysics, the CARMA cirrus microphysics, and the satellite simulator, COSP, used in this study. Steps taken to simulate CAM5 along the ATTREX 3 flight track are also described.

2.3.1. Standard CAM5 Microphysics

The conventional CAM5 model uses a two-moment microphysical scheme, which predicts the mass mixing ratio and number concentration. These moments are tracked for both cloud droplets and ice particles (Morrison & Gettelman, 2008). The standard CAM5 treatment of cirrus is referred to as CAM5/MG from hereafter. The size distributions of cloud ice and cloud droplets within CAM5/MG are represented by gamma functions. Furthermore, the CAM5/MG uses the probability density function (PDF) approach to explicitly represent subgrid cloud water distributions.

Ice cloud fraction ($\mathrm{cf_{ice}}$) is diagnostically calculated within CAM5/MG through a modified version of the Slingo (1987) scheme. A type of relative humidity ($\mathrm{RH_{ti}}$), which is dependent upon total ice water, is used to calculate $\mathrm{cf_{ice}}$. $\mathrm{RH_{ti}}$ is the ratio of total water mass if all condensed water were evaporated into vapor to the water vapor mass at saturation. $\mathrm{RH_{ti}}$ is represented by (equation (1)).

$$\mathrm{RH_{ti}} = \frac{(q_v + q_i)}{q_{\mathrm{sat,ice}}} \tag{1}$$

where q_v is the water vapor mixing ratio, q_i is the ice mass mixing ratio, and $q_{\mathrm{sat,ice}}$ is the saturation mixing ratio over ice. Ice cloud fraction is then calculated from equation (2).

$$cf_{\mathrm{ice}} = \min(1, RH_d) \tag{2}$$

where

$$RH_d = \max\left(0, \frac{RH_{\mathrm{ti}} - RH_{\mathrm{min}}}{RH_{\mathrm{max}} - \mathrm{RH_{min}}}\right)^2 \tag{3}$$

$RH_{\mathrm{min}} = 0.8$ and $RH_{\mathrm{max}} = 1.1$ and are the prescribed minimum and maximum $\mathrm{RH_{ti}}$ thresholds. Note that the $\mathrm{RH_{ti}}$ used in the CAM5/MG cloud fraction scheme is not the same thing as the RH with respect to ice (RHi) presented later in this paper. RHi follows the traditional definition of RH, which is the ratio of the partial pressure of water vapor to the equilibrium vapor pressure at a given temperature.

Primary ice crystal nucleation within CAM5/MG follows Liu et al. (2007). This scheme includes homogeneous freezing of sulfates and heterogeneous immersion freezing on mineral dust based upon work by Liu and Penner (2005). In brief, homogeneous nucleation of ice crystals occurs after exceeding a RH threshold that is a function of temperature and updraft velocity (Liu et al., 2007). Heterogeneous nucleation follows classical nucleation theory (Pruppacher et al., 1997).

Detrained ice is defined as ice crystals deposited directly into the UT by the lateral spreading of convective cores. The size distribution of detrained ice in CAM5/MG is represented by a gamma function. The mean volume radius for cloud droplets and ice is assumed to be 8 and 32 μm, respectively (Morrison & Gettelman, 2008). Detrained ice is handled by bulk convective parameterizations. At temperatures colder than −20 °C all detrained condensate is considered ice. Above 0 °C all ice mass is considered to be in the liquid phase. In between 0 and −20 °C a temperature-dependent linear combination of ice and liquid is assumed (Bardeen et al., 2013).

Lastly, aerosols used for ice nucleation in CAM5/MG are provided by a modal aerosol model (Liu et al., 2012). The modal aerosol model has two different representations, a seven mode (MAM7) model and a three mode (MAM3) model. The primary difference between the two representations is that MAM3 assumes (1) primary carbon is internally mixed with secondary aerosols; (2) coarse dust and sea salt modes are merged into a single mode based on the assumption that dust and sea salt are geographically separated. The same is assumed for the fine dust and sea salt mode; (3) ammonium is prescribed because sulfate is partially neutralized ammonium (Liu et al., 2012). MAM3 is the default aerosol model within CAM5/MG.

2.3.2. CAM5/CARMA Cirrus Model

CARMA resolves the CAM5/MG ice size distribution into 28 size bins that increase in mass by a factor of 2.055 between neighboring bins. CARMA bins start at a size of ~0.5 μm and go up to a size of approximately 1,000 μm for detrained ice and 300 μm for in situ ice. Altogether there are 84 bins for ice because CARMA tracks both the ice formed in situ and the mass of the aerosol on which the in situ ice forms, as well as detrained ice.

CARMA replaces the CAM5/MG ice microphysics in CAM5, but CAM5/MG still handles the liquid cloud microphysics (Bardeen et al., 2013). This parameterization nucleates ice based off of temperature and water activity. Perturbations to temperature within the Koop et al. (2000) scheme can be caused by resolved gravity waves within the simulation. Ice is assumed to be hexagonal in shape based on subvisible cirrus observations from the Cloud Particle Imager instrument taken at temperatures between 198 K (−75 °C) and 188 K (−85 °C; Lawson et al., 2008). An aspect ratio of 1/3 (length/diameter) and a bulk density of 0.917 g/cm^3 are assumed for in situ ice. While the version of CARMA used in this study makes this hexagonal habit assumption, other considerations for ice habit and density could be used. Heymsfield (1986) found TTL cirrus particle habits were dominated by trigonal plates and hollow columns at temperatures of ~190 K (−83 °C) over the Marshall Islands. Murray et al. (2015) further showed that stacking disorders within ice (i.e., cubic sequences within a hexagonal structure) can be a cause for the occurrence of trigonal ice crystals and that over time these trigonal habits were shown to relax into hexagonally shaped crystals (Murray et al., 2015; Yamashita, 1973). Recently, Woods et al. (2018) showed that quasi-spheroids were the dominant shape for small ice crystals at temperatures less than 203 K (−70 °C) over the TWP ocean.

The sulfate particles used for nucleation are prescribed from a climatology produced by English et al. (2011) who used the Whole Atmosphere Community Climate Model with CARMA aerosol microphysics. The mass of sulfates used as ice nuclei within CARMA is binned and tracked. As a result, CARMA keeps track of how much sulfate mass is bound up within ice crystals at any given time. However, CARMA does not update the climatology sulfate population because it is assumed that only a small fraction of the total sulfate aerosol population freezes into ice crystals. As a result, the amount of sulfate released by processes such as sublimation is no longer known to CARMA at the beginning of the next time step.

CARMA uses a semi-implicit tridiagonal vertical transport equation stable for all hydrometeor fall velocities based on a piecewise polynomial method (Colella & Woodward, 1984). As a result, snow in CARMA is prognostic. No autoconversion of ice to snow occurs. Instead, “snow” fills the largest ice bin and CARMA calculates sedimentation velocities for each size bin. Ice/snow remain in each bin until it has fallen all of the way to the surface. This differs from CAM5/MG, which calculates time rates of the change in cloud water/ice mixing ratio and number concentration using a forward differencing scheme in the vertical dimension. The two models further differ in their treatment of snow as CAM5/MG performs the autoconversion of ice to snow when ice particles reach 400 μm in diameter. CAM5/MG then assumes that snow will fall to the ground within one time step.

Detrained ice mass in CAM5/CARMA uses the same bulk convective parameterizations in CAM5. The primary difference is that CARMA transforms the two-moment detrained ice from CAM5 into a temperature dependent bin distribution. CARMA applies a spherical mass-diameter relationship described by equation (8) of Heymsfield et al. (2010) to account for the large range of ice crystal sizes, densities, and habits associated with detrained ice. The Heymsfield et al. (2010) parameterization relates detrained ice mass to particle size, which is then used to populate the detrained ice bins. For transitioning between ice and liquid, CAM5/CARMA assumes the same temperature dependent linear ramp used by CAM5/MG (Bardeen et al., 2013). At the end of each simulation time step the binned CARMA ice mass and number concentrations are converted back into two-moment distributions and fed back to the CAM5/MG physics.

Outside of the TTL, ice clouds typically cover an area smaller than GCM grid boxes. As a result, cloud fraction is used by GCMs to represent the portion of each grid box covered by cloud. CAM5/CARMA uses the Wilson and Ballard (1999) scheme as discussed by Bardeen et al. (2013) to address this need for a subgrid representation of cloud and supersaturation. Equation (4) shows the Wilson and Ballard (1999) ice cloud fraction scheme:

$$\left.\begin{array}{ll} \mathrm{cf}_{\mathrm{ice}} = 0 & n_{\mathrm{cf}} \leq 0 \\ \mathrm{cf}_{\mathrm{ice}} = 0.5\left(6n_{cf}\right)^{\frac{2}{3}} & 0 < n_{\mathrm{cf}} \leq \frac{1}{6} \\ \mathrm{cf}_{\mathrm{ice}} = 1 - 4\cos^2(\phi) & \frac{1}{6} < n_{\mathrm{cf}} < 1 \\ \mathrm{cf}_{\mathrm{ice}} = 1 & n_{\mathrm{cf}} \geq 1 \end{array}\right\} \tag{4}$$

where

$$\phi = \left\{ \cos^{-1}\left[\frac{3(1-n_{\mathrm{cf}})}{2^{\frac{3}{2}}}\right] + 4\pi \right\}/3 \tag{5}$$

$n_{\mathrm{cf},}$ shown in equation (6), represents the fraction of maximum cloud ice that would be possible if liquid clouds begin to form when the saturation mixing ratio with respect to liquid ($q_{\mathrm{sat,liq}}$) is reached.

$$n_{\mathrm{cf}} = \frac{q_i}{[1-\mathrm{RH}_{\mathrm{crit}}]q_{\mathrm{sat,liq}}} \tag{6}$$

$\mathrm{RH}_{\mathrm{crit}}$ represents the grid box critical RH needed for ice cloud formation. The relationship between n_{cf} and $\mathrm{cf}_{\mathrm{ice}}$ can be seen in Figure 1. As n_{cf} increases, cloud fraction quickly increases within the $0<n_{\mathrm{cf}}\leq\frac{1}{6}$ regime (#2). Within the $\frac{1}{6}<n_{\mathrm{cf}}<1$ regime (#3) $\mathrm{cf}_{\mathrm{ice}}$ continues to increase logarithmically as n_{cf} increases until the maximum value of $\mathrm{cf}_{\mathrm{ice}} = 1$ is reached (#4). The inverse relationship between $\mathrm{RH}_{\mathrm{crit}}$ and cloud fraction can also be inferred from Figure 1. It should be noted that $\mathrm{RH}_{\mathrm{crit}}$ is a tunable parameter within CAM5/CARMA. Sensitivity tests conducted by Bardeen et al. (2013) found that a $\mathrm{RH}_{\mathrm{crit}}$ value of 0.7 produced the most comparable vertical cloud profiles to global CloudSat/CALIPSO observations. Setting $\mathrm{RH}_{\mathrm{crit}}$ to a value less than 1 is necessary for subgrid clouds to form prior to total grid box saturation. However, this value may need to be tuned for other changes in model resolution in future studies.

In order for CAM5/CARMA to allow for both growth and nucleation to occur in only the cloudy subset of the grid box, the subgrid treatment of supersaturation from Wilson and Ballard (1999) is used. Contrary to the subgrid cloud scheme that is used by both CAM5 and CARMA, the subgrid treatment of supersaturation is only used within CARMA. Equations (7) and (8) represent the liquid (S_{liq}) and ice (S_{ice}) subgrid-scale supersaturation ratio, respectively.

$$S_{\mathrm{liq}} = \frac{q_v - \alpha q_{\mathrm{sat,liq}}}{q_{\mathrm{sat,liq}}} \tag{7}$$

$$S_{\mathrm{ice}} = \frac{q_v - \alpha q_{\mathrm{sat,ice}}}{q_{\mathrm{sat,ice}}} \tag{8}$$

where

$$\alpha = \mathrm{RH}_{\mathrm{crit}}(1-\mathrm{cf}) + \mathrm{cf} \tag{9}$$

$q_{\mathrm{sat,ice}}$ represents the ice saturation mixing ratio and cf is overall cloud fraction.

It should be noted that this study does not incorporate heterogeneous freezing into CAM5/CARMA simulations. The CARMA cirrus cloud model currently is only equipped to handle homogeneous freezing.

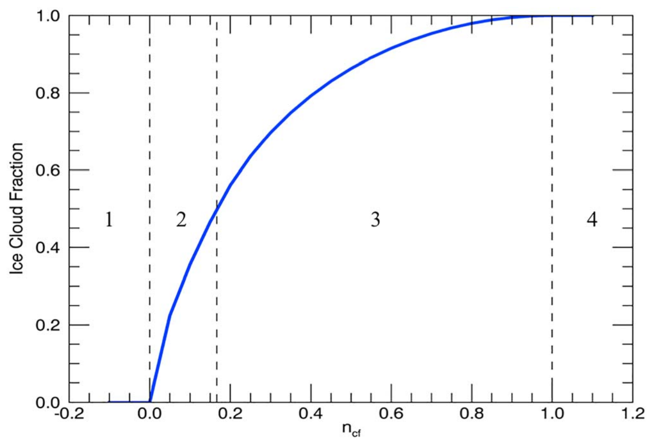

Figure 1. Ice cloud fraction and n_{cf} relationship. The vertical dashed lines and numbers designate each regime from equation (4).

Preliminary studies have shown that the inclusion of heterogeneous freezing has little impact on TTL cirrus clouds in the CARMA model. Froyd et al. (2010) showed that unlike lower altitude cirrus, which form heterogeneously on aerosols such as dust (Cziczo et al., 2013), those in the TTL predominately form on sulfate aerosols. Instead, the dominance of high-frequency waves drives strong cooling events, which promote homogeneous nucleation (e.g., Jensen et al., 2012; Jensen et al., 2016; Kärcher & Ström, 2003). Recent work has made a case for crystalline ammonium sulfate or glassy organics serving as suitable heterogeneous ice nuclei in the TTL, but observations of these aerosol species are still too limited (Jensen et al., 2018).

A summary of all of the simulations used within this study is shown in Table 1 alongside the simulated average tropical cloud fraction at 100 hPa. Further descriptions of each simulation will appear in later sections.

2.3.3. Simulating ATTREX 3 and Satellite Observations

To better compare with observations from the Global Hawk aircraft, the simulations were performed at a 1 × 1° (110 km × 110 km near the tropics) resolution instead of CAM's default 2 × 2° resolution. The model did not need to be retuned after changing resolution because of the nature of a specified dynamics simulation. The high-resolution simulation was chosen because previous studies have shown that horizontal scales of tropical cirrus are often ≥100 km (e.g., Massie et al., 2010; Pfister et al., 2001). Thus, one would expect the high-resolution simulation to reduce the inherent sampling discrepancy when comparing aircraft observations with GCM simulations. Furthermore, all of the simulations were run with specified dynamics (Lamarque et al., 2011). In the specified dynamics simulations, the model was nudged toward Goddard Earth Observing System Model, Version 5 (GEOS-5) reanalysis data. The nudging was composed of a correction factor of 1% of the difference between the GEOS-5 reanalysis data and the model data. At the end of each simulation time step (30 min) the 1% correction was applied to each model level to the simulated wind, surface stresses, latent heat, specific heat, and temperature fields. All other fields were left unconstrained. MERRA 2 reanalysis data was tested in place of GEOS-5 due to its improved representation of the cold point tropopause (Molod et al., 2015), but no significant difference was noted.

To simulate ATTREX 3 flight tracks, history files containing the aircraft's location were created. During the simulation, flight track information was converted to 1-min averages. The model used this averaged flight track information to determine the geographic location of the aircraft at a given time. In the post simulation analysis, the aircraft location was used to perform a weighted interpolation of the four closest horizontal grid boxes. This value was then averaged with the weighted interpolation value from the previous time step. As a result, four grid cells and two time steps (eight grid cells in total) were used in each interpolation to obtain a singular value at the aircraft location at a given time within a flight. Weighted averaging was performed because the aircraft is not confined to a single grid box or may only traverse a portion of the model grid box in a given time step (e.g., the bottom corner).

For comparison of the model with satellite observations, the aforementioned satellite simulator known as COSP was used. COSP outputs a unique set of model fields that allow for a direct comparison with satellite retrievals (Kay et al., 2012). COSP possesses a number of satellite simulators unique to each satellite and its respective instruments (e.g., Moderate Resolution Imaging Spectroradiometer, CALIPSO, and CloudSat). Grid box mean vertical profiles of temperature, humidity, cloud optical thickness, emissivity, and mixing ratios of clouds and precipitation from CAM5 are supplied to each simulator within COSP where instrument specific models simulate signals and/or retrievals of the satellite instruments (Bodas-Salcedo et al., 2011). The power of COSP is that the resulting output diagnostics possess statistics and quantities similar to the actual observations, thus making them directly comparable to the data measured by satellite instruments rather than the derived variables produced by the retrieval algorithms (Bodas-Salcedo et al., 2011). It should be noted that though CARMA and COSP are separate modules that couple with CAM5, they are compatible with one another. The execution of COSP occurs at the end of each time step after all physical processes have concluded in the simulation. Thus, CARMA will have already modified the ice clouds and relayed this information to CAM5 prior to the execution of COSP.

Table 1
Summary of CAM5 Simulations

Simulations	CARMA	Cloud fraction = 1 above 120 hPa	RH_{crit} = 1 above 120 hPa	Cold point tropopause reduced by 2 K	Random gravity waves (anomaly in kelvins)	Tropical average 100-hPa cloud fraction [%] (CAL-LV2 ~ 18)
CAM5/MG[a]						1.6
CAM5/CARMA[b]	X[c]					6
MG-2K[d]		X		X		3
CF1-2K[e]	X	X	X	X		21
RW1K[f]	X	X	X	X	X(1.0 K)	23
RW2.2K[g]	X	X	X	X	X(2.2 K)	30

Note. CARMA = Community Aerosol and Radiation Model for Atmospheres; CAM = Community Atmosphere Model.
[a]The standard CAM5 model. [b]The coupled CAM5 and CARMA models. [c]The symbol "X" denotes a deviation from the default Morrison and Gettelman (2008) cloud scheme. [d]The standard CAM5 model with the CF = 1 and cold point temperature modifications. [e]The coupled CAM5 and CARMA models with the CF = 1 and cold point temperature modifications. [f]The CF1-2K case with a 1.0-K temperature perturbation in the tropical tropopause layer. [g]The CF1-2K case with a 2.2-K temperature perturbation in the tropical tropopause layer.

3. Results

3.1. TTL Cloud Layer(s)

To ensure consistency between observations and the simulations along the flight track, observations were confined to the altitudes at which the CPL consistently observed cloud layers (13.5–17 km, Figure 2). The 16 January transit flight was omitted from the data because there are no NW data for that day. Figure 2 shows an example of the cloud layer from research flight one (RF01). This flight occurred on 12–13 February and performed a north-south survey of the TWP. The flight track initially arced north and west of Guam and then reversed course eventually heading south of Guam down to near the equator. Most of the cloud observations taken during this flight were of in situ formed cirrus except during the southernmost extent of the flight where convection was encountered (Jensen, Pfister, et al., 2016). Along the flight track (black line, bottom panel) the NW saw instances where the aircraft was in cloud (red line, bottom panel) between 13.5 and 17 km. The gray shaded boxes in Figure 2 show where a number of CPL 532-nm backscatter images (Figure 2, top panel) occurred during the flight. Each CPL segment shows a persistent 1- to 2-km-thick cloud layer between 15 and 17 km. At times, there is a second more optically thick, patchy cloud layer associated with convection between 13 and 15 km. It should be mentioned that there may be cloud above the high, persistent cloud layer where the CPL image shows none. The yellow line in the top panel of Figure 2 shows the approximate Global Hawk altitude within each CPL snapshot. The downward facing CPL would miss any cloud at or above this level. Lastly, the contours in the bottom panel of Figure 1 show the CAM5/MG simulated cloud fraction along the aircraft flight track. Comparisons with NW in-cloud instances show that outside of when the Global Hawk was in close proximity to convection, CAM5/MG greatly underrepresents the times when cloud is present.

The Global Hawk stayed within these cloud layers in the TTL on average for 5 min at a time. Observations were grouped into 5-min averages in response. Descent and ascent rates of the Global Hawk varied greatly during the mission, but on average the aircraft descended at a rate of 5 m/s and ascended at a slower rate of 3 m/s. For a 5-min period that means that the aircraft has descended/ascended approximately 1,500 m/900 m. Thus, in a 5-min span one could expect the Global Hawk to have traversed one of the two cloud layers observed in the TTL. Considering the Global Hawk's true airspeed of 170 m/s, a 5-min averaging period also means that the horizontal extent covered by the aircraft was approximately 51 km, or half of a model grid box.

Other averaging periods were experimented with to make certain that the data were not significantly biased by having a period that is so short that only cloudy or cloud-free cases occurred, or so long that aircraft altitude changes biased the statistics. Figure 3a shows the impact that different averaging periods have upon the mission cloud frequency statistics from the NW instrument along the aircraft flight track. For a 5-min averaging period, NW observes full cloud cover (CF > 0.95) approximately 41% of the time and clear-sky conditions (CF < 0.05) 24% of the time. The remaining 35% of the observations showed intermittent cloud cover (0.05 < CF < 0.95). The shorter averaging period of 2 min yielded higher occurrences of complete cloud cover

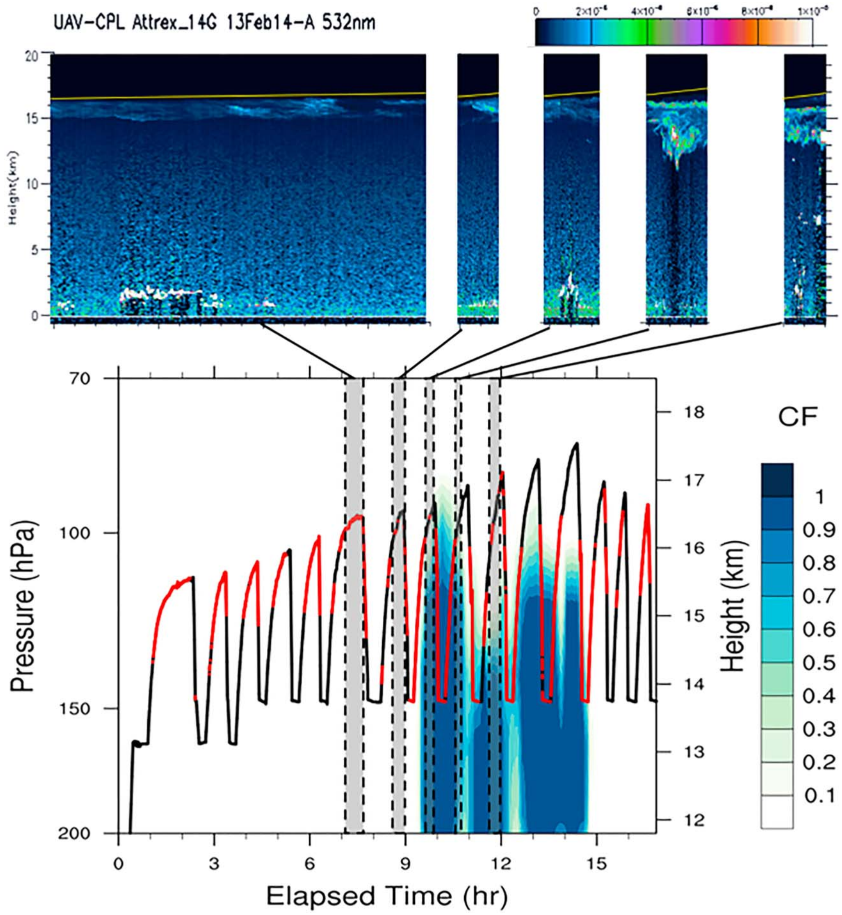

Figure 2. CPL 532-nm backscatter images of portions of science flight RF01 (top panel). The yellow line in each panel shows the aircraft altitude during each flight segment. The RF01 flight track is shown in the bottom panel (black line) with in-cloud instances observed by the National Oceanic and Atmospheric Administration Water instrument highlighted in red. Gray shading shows the portion of the flight track covered by each CPL image. A curtain of simulated CAM5/MG cloud fraction is also shown in the bottom panel. ATTREX = Airborne Tropical Tropopause Experiment; CPL = Cloud Physics Lidar; CF = cloud fraction; UAV = unmanned aerial vehicle.

(~50%) and clear-sky conditions (~28%) when compared to the longer sampling times. The 2-min averaging period registered partially cloudy conditions for only 22% of observations confirming that a shorter averaging period returns predominantly cloudy or clear-sky cases. The longer averaging times of 8 and 10 min show similar statistics to the 5-min sampling case. For an 8-min averaging period, NW observations indicate full cloud coverage approximately 35% of the time and clear-sky conditions approximately 21% of the time. Intermittent cloud cover occurred 44% of the time. The 10-min averaging period has slightly fewer total cloud observations (32%) and clear-sky observations (~20%). As a result, the longest averaging period had the most intermittent cloud cover (~48%). The longer averaging periods show a reduction in the two cloud fraction extremes. This reduction is likely a reflection of the aircraft changing altitudes as the Global Hawk would have ascended/descended distances greater that the 1- to 2-km cloud layer thicknesses. As a result, instances of cloudy and clear-sky will have been erroneously averaged together, leading toward more intermittent cloud cover. Taking into account the Global Hawk ascent/descent rates and results from this averaging period analysis, 5 min is the best choice of averaging time for the cloud fraction statistics.

Note that only observations taken at ≤205 K are used in the ATTREX 3 flight comparisons. This step was taken in order to only include observations taken while the Global Hawk was at cruise altitude in the UT. Likewise, the simulation results also use this temperature threshold.

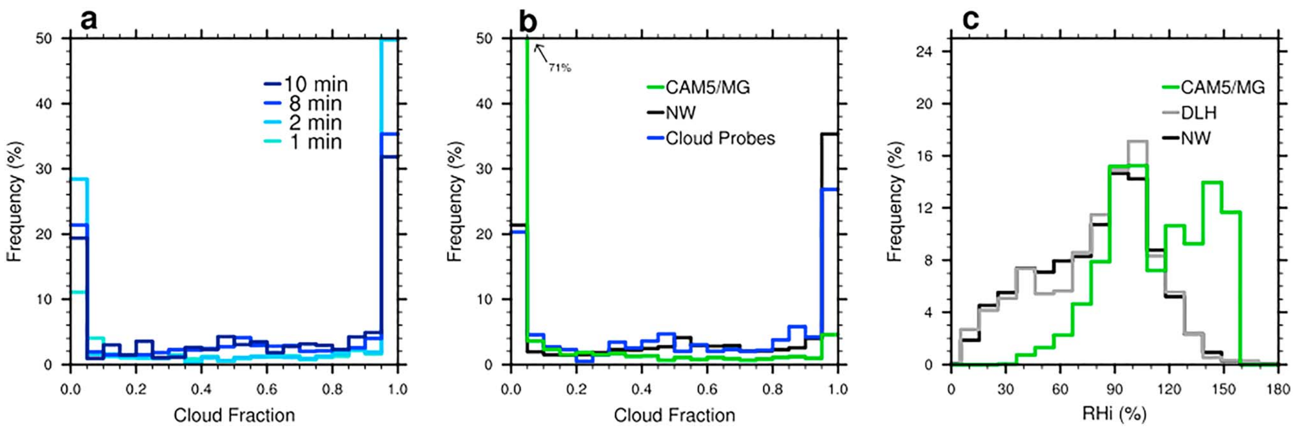

Figure 3. NW mission averaged cloud fraction frequency observations are shown in panel (a) for various averaging periods. The 2-min averaging (turquoise), 5-min averaging (light blue), 8-min averaging (blue), and 10-min averaging (dark blue) periods are shown. Mission averaged cloud fraction frequency and relative humidity with respect to ice frequency observations along the flight track are shown in (b) and (c), respectively. For panel (b), observations from the NW instrument (black) and combined cloud probes (blue) are compared to the CAM5/MG simulation (green). The value in the upper left corner provides the simulated clear-sky frequency. Panel (c) compares the CAM5/MG simulation to observations from the DLH (gray) and NW (black) instruments. Only data at temperatures ≤205 K (~190 hPa) are considered. NW = National Oceanic and Atmospheric Administration Water; DLH = diode laser hygrometer; CAM = Community Atmosphere Model.

3.2. Simulations Using the CAM5/MG Model

Figure 3b compares mission averaged cloud frequency from the aforementioned NW instrument and the summation of H-2DS and either H-FCDP or S-FCDP observations with simulations from the CAM5/MG model. The choice of which FCDP instrument to use was based upon which probe was deemed to provide more reliable observations for each flight. In-cloud instances for both sets of observations are defined as any time when the observed IWC was greater than zero. The results for the CAM5/MG simulation along the ATTREX 3 flight track is also shown in Figure 3b.

NW and cloud probe observations show similar cloud cover along the flight track. Approximately 31% of the cloud probe observations show greater than 95% cloud coverage compared to NW's 38%. The amount of clear-sky conditions observed by the cloud probes (21%) is within 3% of NW observations. Intermittent cloud coverage observed by the cloud probes (48%) occurs 13% more often than NW instrument (35%). Overall, the cloud probes see more broken cloud cover than NW, but that is likely due to differences in instrument sensitivity.

The CAM5/MG simulation differs considerably from the observations in that it shows clear-sky conditions approximately 71% of the time. The CAM5/MG simulation shows partially cloudy skies along the flight track 25% of the time. Full cloud coverage occurs approximately 4% of the time. The cloud fraction frequency distribution in the Figure 3b is consistent with the low tropical 100-hPa cloud fraction average of 1.6% from Table 1 and confirms that the CAM5/MG simulation produces too few clouds along the ATTREX 3 flight track.

Figure 3c shows the RH with respect to ice (RHi) frequency distribution for the ATTREX 3 mission. Both sets of observations have similar distributions with a peak near saturation and only minor discrepancies in RHi across the distributions. In contrast to the observations, the CAM5/MG simulation has multiple modes in its RHi distribution. The first simulation mode occurs within 10% RHi of saturation and has a similar frequency of points (31%) to that of the NW (29%) and DLH (33%) observations. The CAM5/MG case also has peaks near 130% and 150% supersaturation. There are very few instances of observed RHi above 130% (<5% of the time) in the 5-min averaged data. The simulated high supersaturations are likely a result of the low cloud frequency in the TTL. Without enough ice crystal nucleation and growth, water vapor is not removed from the air and high supersaturations can persist.

3.3. Base Case: CAM5/CARMA Simulation

The base case uses the previously described CARMA cirrus model. The CAM5/CARMA simulation produces almost no locations along the flight track with more than 40% cloud cover (Figure 4a). However, the fraction

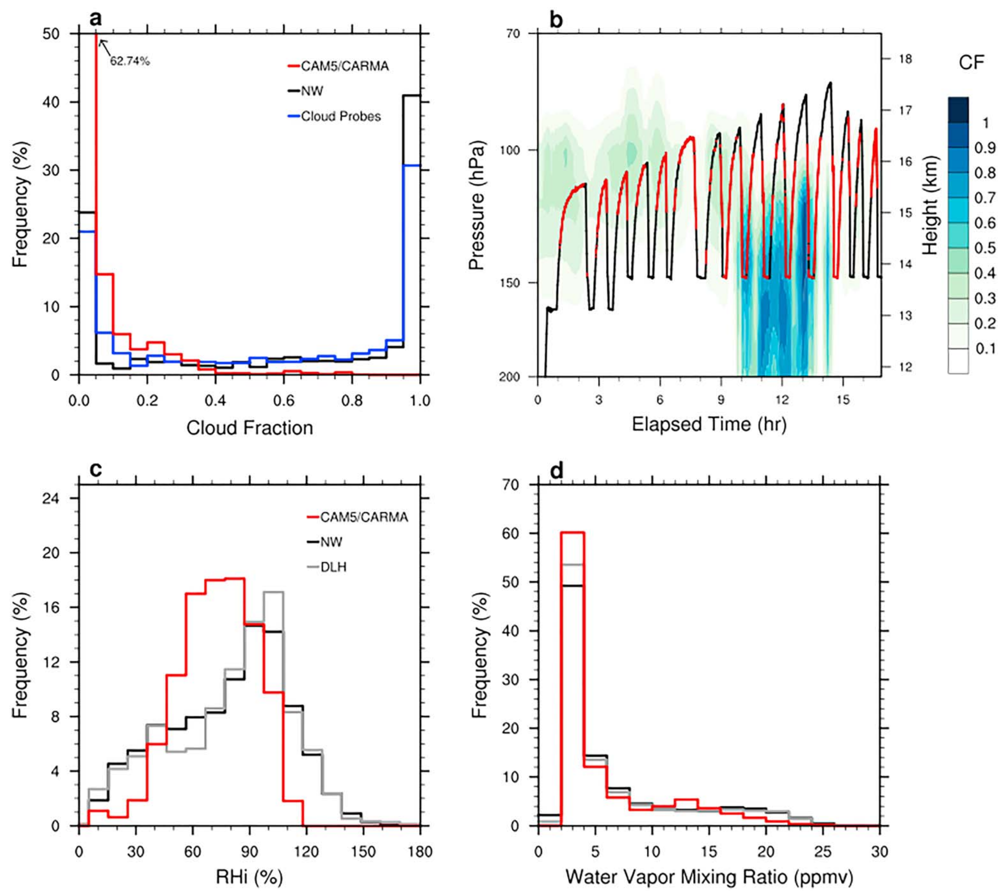

Figure 4. (a) The same as Figure 2b but for the CAM5/CARMA base case simulation. (b) The CAM5/CARMA base case cloud fraction curtain (contours) along the Airborne Tropical Tropopause Experiment 3 flight track (black line) during RF01. The red line in panel (b) denotes instances NW indicated the aircraft was in cloud. (c) The same as Figure 2c but shows the CAM5/CARMA base case simulation. (d) The mission averaged water vapor mixing ratio frequency distribution. Panels (c) and (d) use the same legend. NW = National Oceanic and Atmospheric Administration Water; CF = cloud fraction; DLH = diode laser hygrometer; CARMA = Community Aerosol and Radiation Model for Atmospheres; CAM = Community Atmosphere Model.

of cloud-free grid cells is nearly 9% less than in the CAM5/MG case. Figure 4b shows the RF01 flight track from Figure 2 overlaid onto the CAM5/CARMA simulated cloud fraction curtain. The CAM5/CARMA simulation is markedly different from the CAM5/MG in Figure 2 as cloud fractions between 0.1 and 0.3 are present at many locations along the flight track where the aircraft was in cloud. However, the cloud fraction associated with convection in the southern leg of RF01 is 0.2–0.4 lower than in the CAM5/MG case. The lack of cloud cover in the CAM5/CARMA simulation is likely a result of the low humidity shown in Figure 4c. The CAM5/CARMA RHi frequency distribution shows a monomodal distribution which is similar to the observations unlike the CAM5/MG case shown in Figure 3c. However, the distribution of the RHi for the CAM5/CARMA simulation has a single peak between 60% and 90% saturation, which is low relative to the data. Even though the CARMA model does not include heterogeneous nucleation, while the MG model does, the CARMA model does not show supersaturations above 120%. Since CARMA only conducts homogeneous nucleation and few clouds have formed, one might expect CAM5/CARMA to produce high supersaturations close to the homogeneous freezing threshold of 160%. The reason the model does not produce high supersaturations is due to the previously described subgrid supersaturation scheme and RH_{crit} parameter. Because RH_{crit} is set to 0.7, a supersaturation of 160% for homogeneous nucleation would be scaled within the model to ~112%. This scaling is also a partial reason as to why the RHi distribution is centered nearer to 70%. The simulated RHi crosses the simulation homogeneous nucleation supersaturation threshold ~2% of the time, which is comparable to the observations which exceed 160% ~1% of the time. The frequency distribution of water

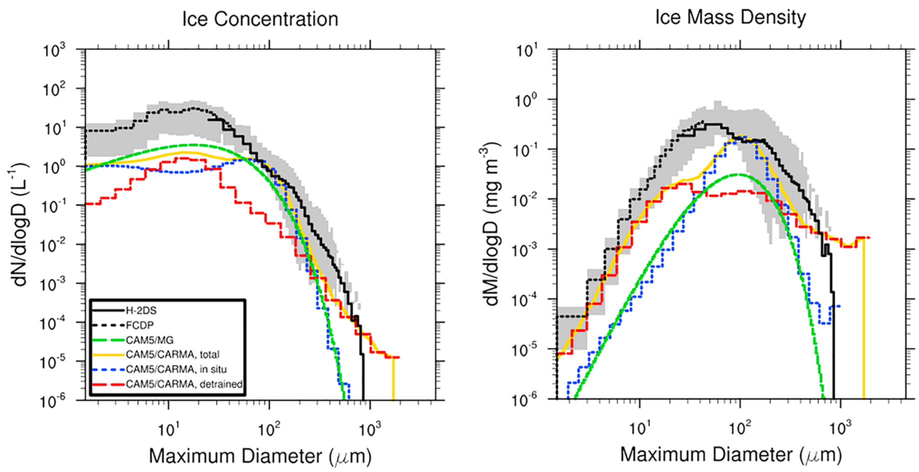

Figure 5. Mission averaged in-cloud ice number concentration (left) and mass density (right) size distributions. Black lines show H-2DS (solid) and the combined H-FCDP and S-FCDP (dotted) observations. The gray shading shows the 25th to 75th quartile range for the FCDPs and H-2DS. The gold, blue, and red lines show the CAM5/CARMA simulation's total ice, in situ ice, and detrained ice, respectively. The green line shows CAM5/MG total ice. FCDP = Fast Cloud Droplet Probe; CAM = Community Atmosphere Model; CARMA = Community Aerosol and Radiation Model for Atmospheres.

vapor mixing ratio is shown in Figure 4d. Both NW and DLH instruments are nearly identical. Approximately 72% (NW) and 75% (DLH) of the observations fall between 2 and 8 ppmv. The CAM5/CARMA case exceeds the DLH observations by 6% at 3 ppmv and 2% at 13 ppmv. The CAM5/CARMA case is low everywhere else but still within 3%. Figure 4 shows that the addition of CAM5/CARMA to CAM5/MG helps improve the occurrence of TTL clouds in the model. CAM5/CARMA nearly has the same amount of water vapor in the TTL as well. However, it is evident from Figure 4 that the simulation still has far too few clouds. Furthermore, an RH_{crit} value of 0.7, which worked well for the 2° × 2° global representation of cirrus (Bardeen et al., 2013), fails in the TTL where a larger RH_{crit} value is needed.

Figure 5 compares the observed mission averaged size and mass distributions with those simulated by the CAM5/CARMA and CAM5/MG models when clouds are present along the aircraft flight track. While in situ and detrained ice retain their native size bin grids converted to maximum length in Figure 5 (see section 1.3.1), total ice is calculated by interpolating both ice fields to a uniform size, 250 bin grid before determining the total value per bin to compare with CAM5/MG. This summation is done for both ice mass and number.

The CAM5/MG simulation consistently underrepresents ice concentration over the whole size distribution by an order of magnitude or greater. Only between 100 and 400 μm does the CAM5/MG simulation reside within or near the lower limit of the H-2DS observational spread. The simulated mass density distribution reveals a similar story to that of the ice concentration. There is too little mass for all particle sizes outside of the 150- to 300-μm range. The simulated distribution is also too narrow and possess a peak mass at a particle size of 100 μm instead of the observed mass peak at 50–60 μm.

The addition of CARMA in the CAM5/CARMA simulation provides a similar size distribution to that of the CAM5/MG case. CAM5/CARMA produces too few ice particles less than 100 μm in size. Between 100- and 200-μm total ice concentration lies within the observational spread and closely follows the H-2DS observations. From 200 to approximately 800 μm simulated total ice concentration remains within the observational spread. The maximum particle size observed by H-2DS is shown to be 850 μm in Figure 5. Beyond this upper limit the model simulation produces ice crystals up to 1,200 μm in size where H-2DS observations see none. CAM5/CARMA produces a similar total ice concentration for sizes smaller than 300 μm to that of the CAM5/MG simulation, but for particle sizes between 300 and 800 μm, CAM5/CARMA has a more comparable ice concentration to the observations. Overall, both the CAM5/MG and CAM5/CARMA simulations appear to be deficient in ice.

The CAM5/CARMA mass size distribution in Figure 5 (right panel) differs from the number size distribution as total ice mass falls within observational variation between 2 to 20 μm when CARMA detrained ice is the dominant ice type. Between 20 and 80 μm the CAM5/CARMA total ice mass falls outside of the lower observational bound. From 80 to 700 μm CAM5/CARMA total ice mass falls within the observational range. CAM5/CARMA possesses a similar mode to that of the CAM5/MG case, but is often a factor of 2 or greater. The tail for particles larger than 1,000 μm is again simulated contrary to the observations and CAM5/MG case. A potential cause for the discrepancy in the largest ice bin between the CAM5/MG and CAM5/CARMA cases is the aforementioned prognostic treatment of snow in CAM5/CARMA (section 2.3.2). CARMA snow is allowed precipitate over multiple time steps instead of being immediately removed. As a result, snow may remain aloft longer, populating the largest number/mass bin. However, that only explains the behavior of the largest bin of the particle tail. A further investigation of other causes for the large particle tail will be discussed in the section 4. Both the ice concentration and mass distributions in Figure 5 reveal that much of the improvements between CAM5/MG and CAM5/CARMA stem from detrained ice. This is due to the switch from the two-moment scheme to the temperature dependent bin distribution described in section 2.3.2.

It might appear to the reader that the CAM5/CARMA simulated number and mass distributions shown are inconsistent. This inconsistency stems from the aforementioned shape and density assumptions for in situ and detrained ice (section 2.3.2). In situ ice has a density equal to the bulk density of ice and is assumed to have a hexagonal plate shape. Detrained ice uses the aforementioned Heymsfield et al. (2010) parameterization, but since cloud particles smaller than 50 μm are approximately spherical in shape (Korolev & Issac, 2003), detrained ice is constrained to not exceed the bulk ice density for those sizes. Therefore, in situ ice for cloud particles smaller than 50 μm will possess less mass than detrained ice of similar maximum diameter due to its shape possessing less volume. Future development to the CARMA cirrus model should reconsider this hexagonal plate shape assumption for in situ ice as a recent study of TTL ice by Woods et al. (2018) has shown that quasi-spheroids dominate in situ ice crystal habits at temperatures ≥203 K.

3.4. Improved Resolution of Tropopause Temperature: CF1-2 K Simulation

From the above results, it is apparent that neither CAM5/MG nor CAM5/CARMA produces sufficient cloud fraction, or RH when compared to ATTREX 3 observations. Nor does either model produce the proper ice distributions. Two sources of error were found that could account for the underrepresentation of clouds in the model simulation. The first source of error is the coarse vertical resolution in the model and reanalysis data (1 km), which hindered the representation of the cold point tropopause. As a result, the grid cell in the simulation that contained the tropopause was often 2 K too warm compared to temperatures observed by Constellation Observing System for Meteorology Ionosphere and Climate (Anthes et al., 2008; Rocken et al., 2000). The warmer temperatures can drive down RH within the TTL, thus suppressing ice nucleation and cloud formation. In response, the simulated cold point tropopause was located by finding the coldest model level between 400 and 10 hPa. The CARMA microphysics were adjusted to be 2 K cooler at that level. The cold point temperature adjustment was executed every time step between 400 and 10 hPa. It is important to note that the temperature adjustment was applied only to CARMA and thus did not erroneously modify the model dynamics.

The second source of error was the previously discussed deficit in simulated cloud cover fraction along the flight track. The Wilson and Ballard (1999) cloud scheme used in CAM5/CARMA is designed for improved weather forecasts in the middle-to-lower troposphere where convection is important and cloud extent is smaller than a GCM grid box. However, as was previously discussed, the cloud coverage in the TTL observed by the CPL during ATTREX 3 was often equivalent in size to that of a 1 × 1° grid box and was often found at pressure levels above convection. As a result, the low cloud fraction calculated via the Wilson and Ballard (1999) cloud scheme would cause small α values in equation (9). The small α would in turn cause the subgrid supersaturation to increase unrealistically. Since all microphysics occurs in-cloud, the small cloud fractions would amplify the nucleation/growth of in-cloud ice crystal numbers, but they would have little impact upon the total grid box water. Due to the high supersaturation within the subset of the grid box, the in-cloud crystals would grow large in size and sediment out of the cloud, depleting the cloudy region of water vapor and suppressing further nucleation. In response to this problem, the model assumptions of cloud fraction and RH_{crit} were modified to reflect clouds covering the entire grid box. Cloud fraction was forced to equal

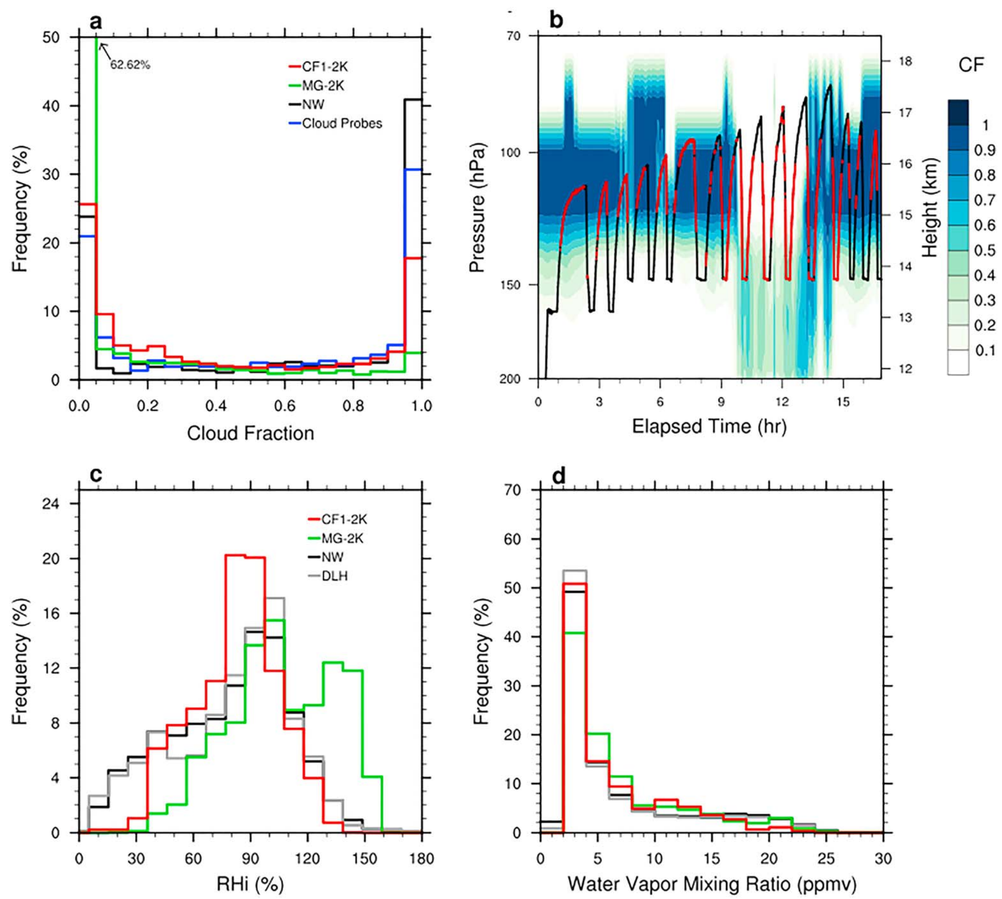

Figure 6. Same as Figure 4 but for the CF1-2K and MG-2K simulations. The cloud fraction curtain in panel (b) is from the CF1-2K case.

1 for altitudes above 120 hPa whenever a cloud was present. Between 140 and 120 hPa a linear ramp of increasing cloudiness which transitioned between the Wilson and Ballard (1999) scheme and the 100% cloud cover adjustment was used. RH_{crit} is similarly modified. At altitudes above 120 hPa, α from equation (9) was scaled to equal a value that would be obtained if RH_{crit} equaled 1. The net effect of this change means that above 120 hPa the grid box saturation is effectively being used by the microphysics. The same linear ramp used for cloud fraction between 140 and 120 hPa is also used to scale α and RH_{crit}. The combination of these modifications allows for a more realistic treatment of TTL clouds based upon CPL observations but does not interfere with the necessary subgrid treatment of clouds needed lower in the atmosphere where convection is more frequent.

The effect these model adjustments (CF1-2K from here on) have upon the simulated aircraft flight track cloud frequency and atmospheric moisture can be seen in Figure 6. A similarly modified CAM5/MG (MG-2K from here on) simulation has also been included in Figure 6. Both the same cold point temperature adjustment and the same cloud fraction adjustment used by the CF1-2K case are used in the MG-2K case. However, because CAM5/MG already uses the grid box average saturation for the microphysics independent of cloud fraction, there was no need to modify the saturation aspect of the cloud fraction scheme like in the CF1-2K case.

The CF1-2K simulation poses a striking difference from the CAM5/MG and CAM/CARMA simulations previously shown. The frequency of completely cloudy regions in the CF1-2K case in Figure 6a has increased to 18%, whereas the frequency of completely cloudy regions was near 0% in the previous simulation in Figure 4a. The MG-2K simulation in Figure 6a has only small changes ($\leq$1%) in cloud fraction in cloudy regions relative to the CAM5/MG simulation in Figure 3b. Conversely, instances of clear-sky conditions

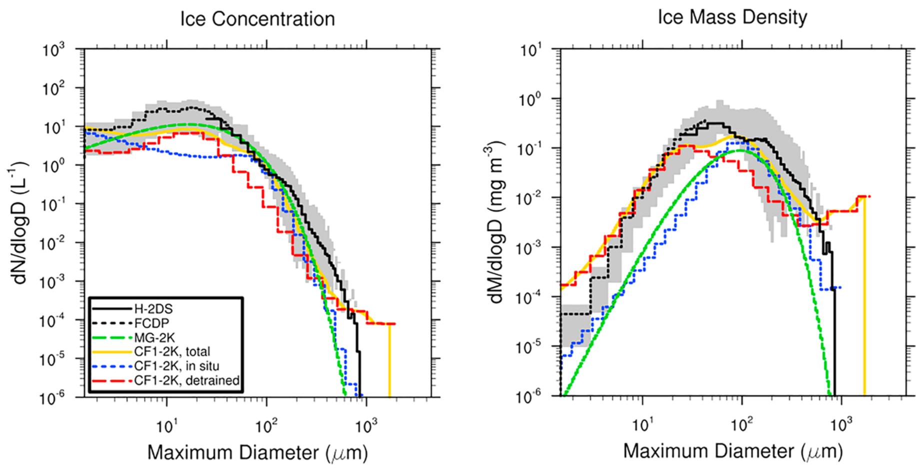

Figure 7. Same as Figure 5 but for the CF1-2K and MG-2K simulations.

have been reduced to ~26% in the CF1-2K simulation, which is within 5% of both the NW and cloud probe observations. The MG-2K simulation experiences a smaller change in the clear-sky frequency with a ~9% reduction. The frequency of intermittent cloud cover in the CF1-2K case has also improved to be more comparable with both sets of observations, occurring approximately 56% of the time. The increase in cloud fraction in the CF1-2K simulation is further evident in Figure 6b where significant cloud fractions (>0.7) are simulated in all locations where the CPL saw a persistent cloud layer. Simulated cloud fraction is also in good agreement with the NW instrument's in-cloud observations except between 10 and 13 hr where the cloud fraction simulated near convection has decreased compared to the CAM5/CARMA case.

The CF1-2K case's RHi peak in Figure 6c is shifted to a higher RHi range and is narrower than in the CAM5/CARMA case (Figure 4c). The new RHi peak is centered between 80% and 100% saturation and now more closely resembles observations. Due to the narrowness of CF1-2K simulation's distribution, there are still too few instances at both ends, however. The MG-2K simulation retains the bimodal RHi distribution from the uncorrected case. The only noticeable change occurs between 120% and 130% RHi where a reduction in frequency from 11% to 8% occurs.

While the simulated RHi improved relative to observations, the CF1-2K simulated water vapor mixing ratio failed significantly change from the CAM5/CARMA case (Figure 6d). The only major change to the simulation occurred at 3 ppmv with a reduction in frequency of approximately 9%. The shape of the MG-2K distribution is comparable to the observations and the CF1-2K case. However, the frequency of instances at 3 ppmv is only 41% in the MG-2K case. Between 4 and 8 ppmv the MG-2K simulation exceeds the observations by a total of 10%. There is little change between the CAM5/MG (not shown) and MG-2K cases. Overall, the CF1-2K simulation better represents cirrus cloud frequency along the ATTREX 3 flight track and has an improved RHi distribution, while the MG-2K simulation shows little to no improvement.

The size and mass distributions for the CF1-2K and the MG-2K cases are shown in Figure 7. Compared to the CAM5/CARMA simulation without the correction, there is an increase of nearly an order of magnitude for the total concentration of ice particles smaller than 30 μm with half of an order of magnitude increase in ice concentration between 30 and 100 μm. Below 100 μm, the CF1-2K concentration simulation now falls within observational error. Simulated total ice concentration for particles larger than 100 μm remain within error bars of observations and remain largely unchanged from Figure 5. The main improvement in total ice concentration is associated with in situ ice produced by CARMA, which increased by as much as one and a half orders of magnitude for ice crystals smaller than 100 μm. Detrained ice concentrations also see an increase for ice crystals smaller than 100 μm. The MG-2K simulation exhibited a similar improvement that results in a distribution akin to that of the CF1-2K in situ ice except for particles larger than 300 μm.

The CF1-2K mass distribution in the right panel of Figure 7 also exhibits an increase in ice for particles smaller than 100 μm proportional to the changes in the ice concentration. The CF1-2K total ice mass lies within observational spread for most of the distribution with outliers at 60- and <5-μm-sized particles.

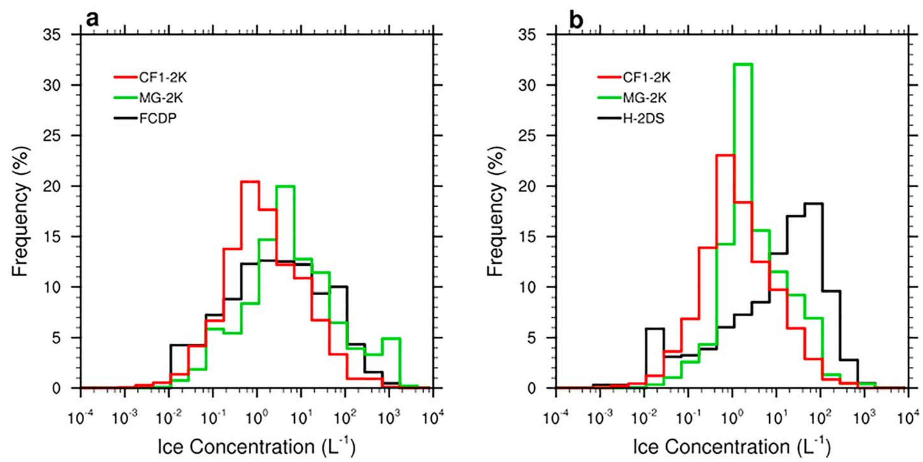

Figure 8. Ice concentration frequency distributions separated by cloud probe size range. (a) Ice concentration for the Fast Cloud Droplet Probe (FCDP) size range (1 to 50 μm) and (b) the H-2DS size range (15–3,000 μm). Observations are shown in black, while the CF1-2K and MG-2K simulations are shown in red and green, respectively.

The peak of the mass distribution has broadened and is shifted to values similar to observations. The large ice particle tail that occurred in the CAM5/CARMA case is still present in the CF1-2K case. The MG-2K case mass distribution experiences an increase in magnitude as well, but only resides within observational spread between 100 and 400 μm.

A frequency distribution of ice concentration within the FCDP observable size range (1 to 50 μm) is shown in Figure 8a. The observed distribution lies between 0.01 and 2,000 L^{-1} with the most frequent ice concentrations occurring between 0.4 and 20 L^{-1}. The simulated ice concentrations have a similar shape to the FCDP distribution though the frequency of ice concentrations differ. The MG-2K case's mode lies between 1 and 14 L^{-1}. Simulated ice concentrations within this mode occur 13% more often than observations. This mode lies between 1 and 14 L^{-1}. Below the 1 L^{-1} concentration the MG-2K case consistently underrepresents ice by 2–4%. The frequency of high number concentrations (>100 L^{-1}) within the MG-2K case is overestimated by 7% when compared to the FCDP. The CF1-2K case's mode lies between 0.2 and 3 L^{-1}. Within the 0.2 to 20 L^{-1} range, the CF1-2K simulation overestimates the FCDP by ~16%. At concentrations between 20 and 200 L^{-1} the CF1-2K case is consistently below the FCDP observations by >2%, but at all other locations along the distribution the CF1-2K simulation is within 2%.

Like the FCDP, the H-2DS distribution in Figure 8b lies between 0.01 and 2,000 L^{-1}, but it possesses a mode at a higher concentration between 20 and 100 L^{-1}. Both simulations possess noticeably different shaped distributions for the H-2DS size range (15 μm to 4 mm) when compared to the observations. Approximately 71% of the MG-2K simulated ice concentration can be found in a single mode between 0.4 and 6 L^{-1}. Within this same concentration band lies the primary mode of the CF1-2K simulation with a total ice concentration frequency of 53%. Both simulations overshoot the H-2DS observed ice by more than 30% within this mode. Above the 20 L^{-1} mark both simulations possess too few instances of ice concentration. The MG-2K simulation consistently underestimates observations at ice concentrations less than 0.2 L^{-1}. Conversely, the CF1-2K simulation overestimates the observations within this concentration range except at very low concentrations (0.01–0.03 L^{-1}) where the H-2DS has a small mode. The distributions in Figure 8 show that both modified simulations perform better at reproducing the ice crystal concentrations within the FCDP size range than they do with the H-2DS size range. It was previously mentioned and shown in Figure 7 that the CF1-2K modifications promote more nucleation of small ice crystals. Therefore, one would expect better agreement with the FCDP, which can only observe ice crystals up to 50 μm in size, compared to the H-2DS's larger observable range which goes up to 4 mm in size.

Simulated in-cloud extinctions from CAM5/CARMA, CAM5/MG, and CF1-2K are compared to CALIPSO Level 2 product (CAL-LV2) and H-2DS observations in Figure 9. The MG-2K case is excluded because

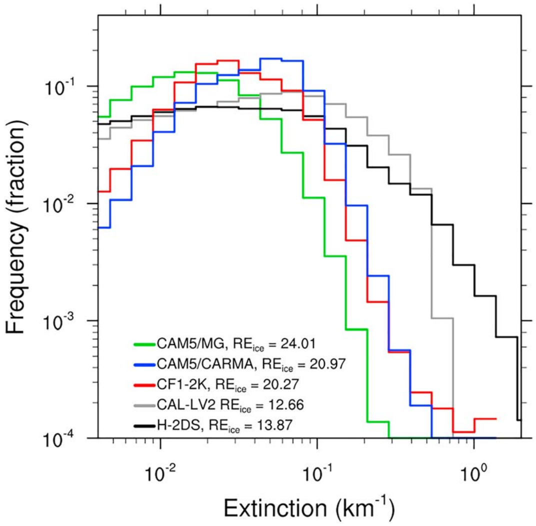

Figure 9. Airborne Tropical Tropopause Experiment 3 mission average extinction frequency distribution. Observations from the Cloud-Aerosol Lidar and Infrared Pathfinder Satellite Observations satellite and H-2DS are shown in gray and black, respectively. The CAM5/MG simulation is shown in green, while the CAM5/CARMA simulation and the modified CF1-2K simulation are shown in blue and red respectively. The mission averaged effective radius is included in the legend. CAM = Community Atmosphere Model; CARMA = Community Aerosol and Radiation Model for Atmospheres.

there was little change in the extinction distribution from the CAM5/MG case. The H-2DS directly calculates extinction from its observed size distributions. Coordinated CALIPSO-aircraft overpasses were limited during the mission. As a result, the CAL-LV2 distribution in Figure 9 encompasses the entire ATTREX 3 region (135°E to 165°E and 5°S to 20°N) during the mission timeframe. An upper backscattering ratio boundary of 0.019 $sr^{-1}\cdot km^{-1}$ is used in the CAL-LV2 observations to remove optically thick convective clouds and to remain consistent with Jensen et al. (2016). Satellite and H-2DS extinction observations are within a factor of 2 to one another everywhere except for the largest extinction values (>0.5 km^{-1}) where the H-2DS probe observed optically thick clouds and CAL-LV2 observed none. Differences in the observed extinction distributions are likely attributed to sampling biases associated with the Global Hawk aircraft. The upper TTL was only sampled later in the mission. As a result, more observations of the lower-middle TTL were collected by the Global Hawk than of the higher regions, which likely led to the high extinction bias in the H-2DS observations (Jensen, Ueyama, et al., 2016).

Extinction from the simulations is calculated from simulated ice size distributions and cross-sectional area assumptions. Detrained ice assumes a spherical cross-sectional area, while in situ ice uses the cross section for randomly oriented hexagonal columns from Hong (2007). The CAM5/MG case possesses too many instances of optically thin clouds with the largest overestimation occurring at ~0.02 km^{-1}. The CAM5/MG peak completely falls off at 0.3 km^{-1} while decreasing at the same rate as the CAM5/CARMA case between 0.1 and 0.3 km^{-1}. The CAM5/CARMA without corrections and CF1-2K simulations both have narrower distributions than the observations. Both CARMA simulations over predict the observed H-2DS extinction peak between 0.01 and 0.09 km^{-1} by as much as a factor of 2. The CAM5/CARMA case's mode is shifted to larger extinction values than the CF1-2K case and is more closely aligned with the CAL-LV2 mode. However, the CAM5/CARMA case is consistently a factor of 2 larger than CAL-LV2 observations.

The mission averaged ice effective radius is presented next to each label in the legend of Figure 9. The CAL-LV2 and H-2DS observations center around 13 μm. In contrast, all three simulations have an average ice effective radius of 20 μm or larger suggesting that the observed extinction is dominated by smaller ice crystals. It is likely that the relative depletion of smaller particles in the simulations is contributing to the lack of large extinction values. We attempt to address this issue in a later section.

From these results, it is apparent that the improved cold point temperature resolution and forced cloud fraction in the TTL improve CAM5/CARMA simulations of observed TTL cirrus cloud frequency and size distributions averaged over the mission. Of these, the change to the diagnosis of cloud fraction in the cloud macrophysics provides the greatest improvement. However, the improved CF1-2K simulation still possesses several shortcomings in its representation of in-cloud ice. For instance, a large particle tail to the mass distribution is computed. The simulations also fail to produce the observed cloud extinction PDF for cases larger than 0.1 km^{-1} and smaller than 0.01 km^{-1}. The causes of and solutions to these issues will be discussed in section 4.

3.5. Simulations Outside the ATTREX 3 Region

So far, only the impact of the CF1-2K modification upon clouds within the ATTREX 3 region has been shown. The CF1-2K simulation has shown improvements in the cloud frequency along the flight track, as well as improvements in the ice concentration and mass distributions. While these results are encouraging, it is also important to consider the larger impacts the CF1-2K adjustments may have upon clouds outside of the ATTREX 3 region. Cloud fraction within the model is involved in calculating radiation balance and thus needs to be correct. Figure 10 shows a multiyear annual average cloud fraction profile for

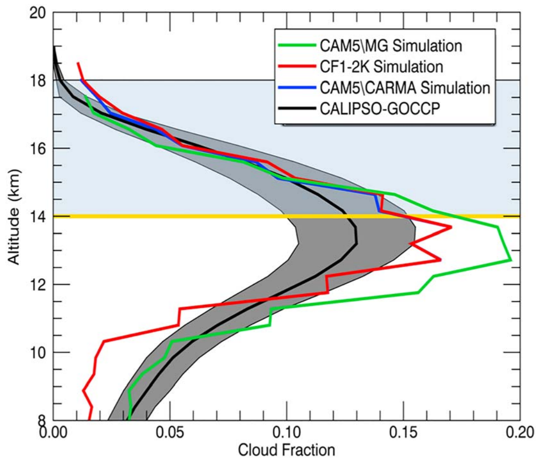

Figure 10. Annual average cloud fraction profile for the tropics (20°N to 20°S). CALIPSO-GOCCP observations are shown in black with a 95% confidence interval (gray shading). Simulations of the CAM5/MG case (green), CAM5/CARMA (blue), CF1-2K (red) are also shown. The tropical tropopause layer region is represented by the light blue shading. The horizontal yellow line shows where the CF1-2K simulation begins to take effect. CAM = Community Atmosphere Model; CALIPSO = Cloud-Aerosol Lidar and Infrared Pathfinder Satellite Observations.

the tropics, defined as 20°N to 20°S. Only cloud fraction values above 8 km are included, which is the approximate average altitude at which CALIPSO becomes fully attenuated. CALIPSO-GOCCP observations are shown by the black line encompassed by a 95% confidence interval in gray. The TTL altitude range as defined by Fueglistaler et al. (2009) is shaded in light blue. The gold line in Figure 10 shows the altitude at which the CF1-2K modifications take effect. The CAM5/MG case in Figure 10 over represents cloud fraction between 11 and 15 km with the largest overestimation of 0.05–0.07 occurring just below the TTL at 13 km. Above and below this range, however, CAM5/MG falls within observational error. Both the CAM5/CARMA simulation and the CF1-2K simulation fall within the observed vertical cloud fraction profile error range within the TTL. Above the lower bound of the TTL, where the model modification is implemented, one can see that the CF1-2K simulation has slightly larger cloud fraction values than the CAM5/CARMA simulation; however, below the TTL, the simulations are nearly identical as the blue CAM5/CARMA line lies directly beneath the red CF1-2K simulation. Above the TTL there is a small presence of clouds (~0.01) in the CARMA simulations, while observations fall to zero. Just below the TTL both CARMA simulations produce 0.01 too many clouds at 12.5 and 13.5 km. Below 11 km both CARMA simulations are biased low by 0.01–0.04. Note that for the CF1-2K case, even though cloud fraction equals one when clouds form, the amount of times when clouds did not form during this multiannual average results in an average tropical cloud fraction within the error bars of the data.

Figure 11 provides another view of the modeled high cloud fraction in the form of global map plots which show the absolute difference between CALIPSO-GOCCP high cloud fraction and simulations (simulation-observation). The CALIPSO-GOCCP high cloud fraction is shown in panel (a) for reference with the global mean high cloud fraction value. High cloud is defined by both CALIPSO-GOCCP and the satellite simulator, COSP, as clouds at pressures below 440 hPa (above ~7 km). While the lower bound of 440 hPa includes clouds below the TTL, the changes do not directly impact clouds below the TTL. Any deviations between simulations will reflect either changes in the high clouds or their indirect effects on lower clouds. The CAM5/MG case in panel (b) shows that CAM5/MG is generally within 0.1 of the observations except in the ITCZ regions with the largest discrepancies occurring over central Africa, the eastern Pacific, and the Western Indian Ocean. In these three regions CAM5/MG over produces high cloud fractions by as much as 0.3. The value next to the panel name provides the mean global bias, which is approximately −0.1 for the CAM5/MG case suggesting too few high clouds globally. The inclusion of CARMA (panel c) increases the global mean bias to −0.147. Though the global bias is worse than the CAM5/MG case, the ITCZ regions where CAM5/MG over represents high cloud have their bias reduced by 0.1. Outside of the tropical region the CAM5/CARMA simulation produces fewer clouds than the CAM5/MG case. The CF1-2K simulation in panel (d) is nearly identical to the CAM5/CARMA simulation. There is a slight improvement in the global mean bias, and the western Pacific Ocean shows a slight increase in cloud cover, but most changes are minor.

The impact the model adjustments have on global annual average longwave cloud forcing (LWCF), which cirrus clouds are known to impact (Ramanathan et al., 1989), is shown in Figure 12. Kay et al. (2012) found that CAM5/MG's global mean LWCF was biased 4 W/m^2 low. Figure 12a shows NASA's Clouds and the Earth's Radiant Energy System's Energy Balance and Filled top of the atmosphere product (Loeb et al., 2018), while Figures 12b–12d again show the global maps of simulation biases. The values next to the panel name represent the global mean LWCF bias. The CAM5/MG simulation shows −2 W/m^2 greater bias than what Kay et al. (2012) found. The discrepancy is likely due to differences between simulations. This study uses a higher horizontal resolution for each simulation, and the CAM5/MG simulation is nudged with GEOS-5 reanalysis data. However, the areas where the CAM5/MG simulation diverges from the observations are similar to those found by Kay et al. (2012).

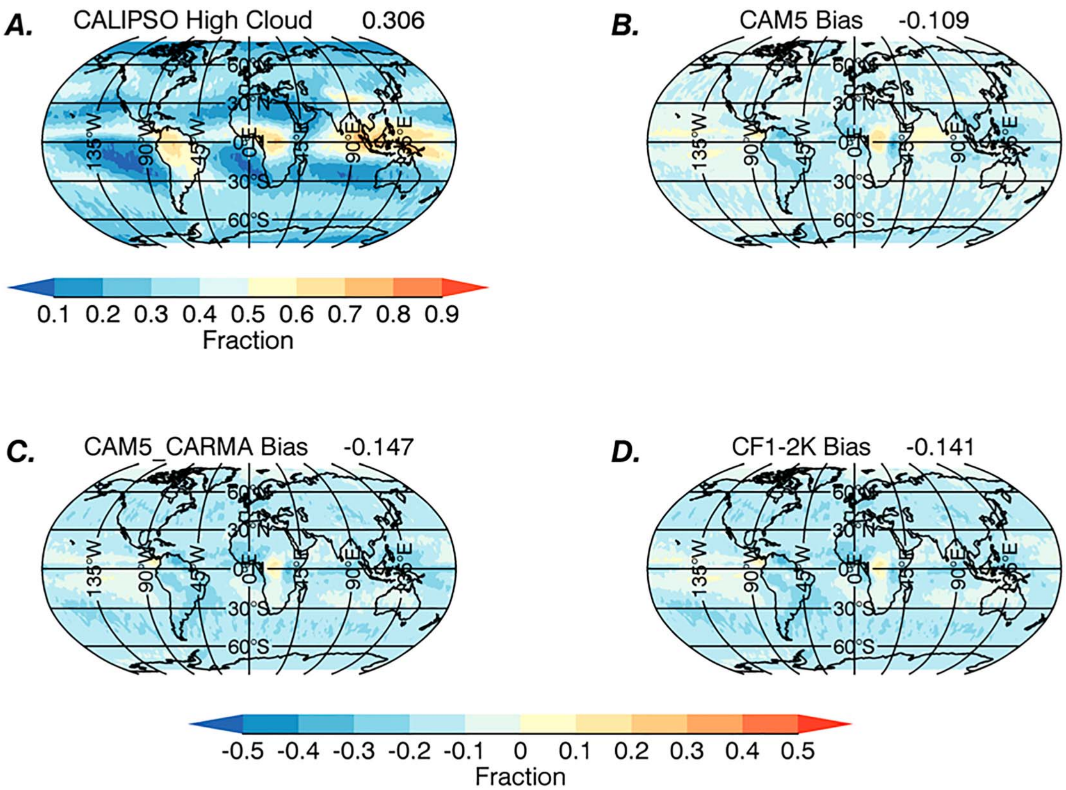

Figure 11. Annual average global high cloud fraction ($P < 440$ hPa) maps. (a) CALIPSO-GOCCP observations. (b–d) Cloud fraction biases (simulation-observation). (b) The CAM5/MG case, (c) the CAM5/CARMA simulation, and (d) the CF1-2K simulation. The number to the right of each panel name provides the global mean cloud fraction average (a) and model bias (b–d). CALIPSO = Cloud-Aerosol Lidar and Infrared Pathfinder Satellite Observations; CAM = Community Atmosphere Model; CARMA = Community Aerosol and Radiation Model for Atmospheres.

Like with cloud fraction, the CAM5/CARMA and CF1-2K simulations both perform slightly worse than the CAM5/MG case and are nearly identical to each other. Both CAM5/CARMA and CF1-2K simulations have a negative LWCF bias of approximately -8 W/m^2. All three simulations again have a positive bias in the ITCZ region and a slightly positive LWCF bias over the poles. The increase in the global negative LWCF bias in the two CARMA cases is related to the reduction in cloud fraction in regions with a positive LWCF bias. This reduction is strongest in the tropics where the largest changes to cloud fraction occurred in Figure 11. For example, the CAM5/MG case exceeded the observed cloud fraction by as much as 0.1 over the Indian Ocean in Figure 11b. The excess clouds led to a positive LWCF bias of 10–15 W/m^2 in the same region in Figure 12b. The introduction of CARMA reduced the positive cloud fraction bias to near zero in Figure 11c. As a result, the LWCF positive bias flipped to a negative bias of 10–15 W/m^2. Therefore, the overall reduction in clouds when CARMA is added is likely the reason for the global decrease in LWCF. The implementation of the CF1-2K modifications provides little changes to these results. This low radiative forcing is also consistent with simulations possessing too few optically thick clouds (Figure 9) and will be discussed in the following section.

4. Discussion

The CF1-2K model adjustment largely addresses the small particle size ice concentration and mass deficiencies exhibited by the CAM5/CARMA model when compared with ATTREX 3 observations without negatively impacting the large-scale cloud fields and radiation balance in the default CAM5/CARMA model. However, some issues with the representation of the TTL cloud fields observed during the ATTREX 3 campaign still remain. While the concentration and mass distributions greatly improved for particles smaller than 100 μm in size, the large particle tail extending to 2 mm still remains unaddressed by the model modifications performed in this study. There are around 10^{-4} particles per liter, or one particle per 10 m^3

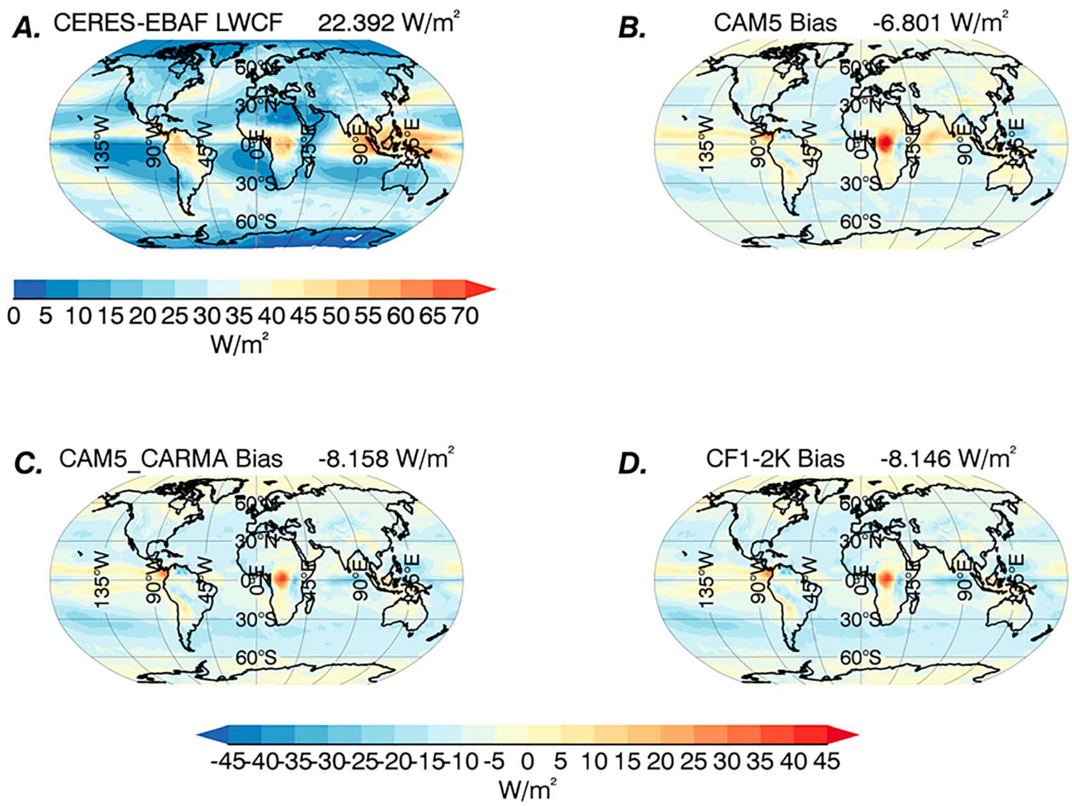

Figure 12. Same as Figure 10 only now LWCF is being shown.

with these sizes. The H-2DS, with a sample size of 10.3 L/s, would not be able to observe such a low concentration of particles. In fact, over the duration of a typical 17- to 20-hr science flight, at most five such particles would likely be detected by the H-2DS. These large ice crystals compose less than 2% of the mass of the cloud. Their direct origin is from detrained ice from nearby cumulus. It is possible that these particles exist but are just too rare to be reported by the cloud probes. It is also important to note that the low concentration of particles larger than 1 mm may be due to sampling bias. The Global Hawk primarily sampled in situ formed clouds and avoided flying in close proximity to convection. Woods et al. (2018) show that many of the large ice crystals associated with convection quickly sediment out and were found away from anvils at lower altitudes during ATTREX 3. Had the aircraft flown closer to convection during ATTREX 3, more might have been observed.

An analysis to find the origins of these particles in the model was undertaken to determine if there was a specific area, flight, or altitude where the excess detrained ice occurred. This analysis led to the discovery that most of the excess detrained ice was confined to aforementioned low, patchy layers of clouds at the base of the TTL between 13 and 15 km (not shown). This is the region where cumulus detrainment is expected to be greatest and is consistent with Woods et al. (2018) findings. Further investigations into convective influence and changes to the shape and behavior of the Heymsfield et al. (2010) size distribution were undertaken but resulted in little impact. Lastly, it is unlikely that ice crystal sedimentation velocity is the source of the large particle tail. As a result, and due to the extreme infrequency of these large particles it is safe to assume that these particles have a negligible impact upon the clouds within the simulations.

Evident from this study's results is that the simulations are missing the large extinction values (> 0.1 km^{-1}) along the ATTREX 3 flight track as shown in Figure 9. The length of time that extinction values larger than 0.1 km^{-1} were observed ranged from ~1 to ~21 min but comprise only ~4% of the total number of H-2DS observations. The CPL observations are inconclusive about the characteristics of the clouds associated with large extinction events as clouds could not be seen by CPL and in situ instruments at the same time. CPL observations that were temporally adjacent to high extinction clouds show nearly cloud free conditions.

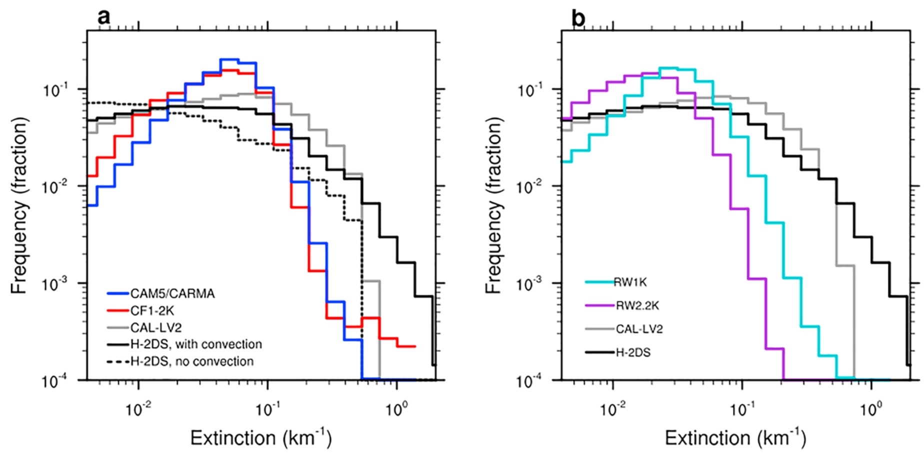

Figure 13. (a) Extinction frequency distributions with convectively influenced flights removed from the CAM5/CARMA (blue) and CF1-2K (red) simulations. H-2DS observations with convective flights removed are represented by the black dashed line. The solid black and gray lines are the same distributions of H-2DS and CAL-LV2, respectively as shown in Figure 8. Panel (b) compares the RW2.2K (purple) and RW1K (turquoise) random temperature perturbation simulations to H-2DS (black) and CAL-LV2 (gray) observations. CAM = Community Atmosphere Model; CARMA = Community Aerosol and Radiation Model for Atmospheres.

Only the 4 and 6 March flights showed any neighboring cloud decks in CPL images. Due to the isolated nature and scarcity of these large extinction events, it is likely that these observations result from a few, optically thick clouds.

One test to determine the source of these isolated optically thick clouds was to remove convectively influenced observations from the H-2DS data set. A back trajectory analysis produced by Leonard Pfister of NASA Ames during the ATTREX 3 mission was used to identify and eliminate science flights, which experienced any observations that were convectively influenced within the last 0.5 days. Note that trajectory error is always a concern in these calculations. There are two fundamental sources of trajectory error for the convective influence calculations. The first is simply due to the tendency for trajectories to diverge with time (see for example, Bergman et al., 2016). The second source of error is due to the inability of global models to consistently capture the mesoscale circulations in the neighborhood of convection due to the coarse grid box representation of convection (a problem shared by mesoscale models, which also often have difficulty placing convection properly). This results in errors in placement of the convectively influenced regions as calculated from trajectories. These errors can occur even when convection is relatively close. Results from removing data influenced by convection in the past 0.5 days are shown in Figure 13a where a dramatic decrease in large extinction events occurs in H-2DS observations. The slope of the H-2DS observations has steepened and the extinction observations cut off at 0.5 km^{-1}. The CAL-LV2 frequency distribution of extinction is unchanged from Figure 9 in Figure 13a because the initial upper extinction limit already eliminates optically thick cloud related to convection. Conversely, the removal of convectively influenced flights shows little impact upon the CAM5/CARMA results. The mode of the CF1-2K simulation shifts from being centered around 0.02 km^{-1} to a larger extinction value of 0.06 km^{-1}, which agrees more with the other data sets. There is also a factor of 2 increase in extinction values larger than 0.4 km^{-1}.

Overall, the removal of observations in close proximity to convection results in closer agreement of large extinction values between the simulations and H-2DS observations; however, they still differ considerably. Also shown by Figure 13a is an insensitivity to the removal of the same convectively influenced flights in the simulation results. One likely cause for such a lack of response is the difference in spatial scale (horizontal and vertical) between GCMs and nature. Further compounding this issue is the fact that the convective scheme can struggle to get the timing and location of convection correct. As a result, not enough ice/water mass reaches the high altitudes investigated in this study, thus causing the muted response to the removal of convectively influenced flights.

Another way to make smaller, optically more efficient ice crystals is to stimulate more nucleation via high-frequency gravity waves. Past studies have shown that gravity waves with periods less than 1–2 days can strongly influence ice nucleation and the formation of cirrus clouds by promoting the formation of small, numerous ice crystals (e.g., Hoyle et al., 2005; Jensen & Pfister, 2004; Jensen, Ueyama, et al., 2016; Kärcher & Lohmann, 2002; Kärcher & Ström, 2003). The increase in number of small ice crystals due to high-frequency waves stimulates an increase in TTL cloud frequency (Jensen & Pfister, 2004; Schoeberl et al., 2015; Ueyama et al., 2015). The increase in TTL ice crystals and cloud frequency does not coincide with an increase in the dehydration of ascending TTL air, however. Due to the small ice crystal sizes and low sedimentation velocities, ice crystals formed from high-frequency gravity waves remain aloft long enough for the warming phase of the wave to sublimate and rehydrate TTL air (Schoeberl et al., 2014; Schoeberl et al., 2015; Schoeberl et al., 2016). TTL waves were observed to be frequently present during ATTREX (Jensen, Pfister, et al., 2016; Kim et al., 2016; Kim & Alexander, 2015; Podglajen et al., 2018).

CAM5/MG and CAM5/CARMA represent vertically propagating gravity waves with a parameterization based upon a combination of work done by Garcia and Solomon (1985), Holton (1982), Lindzen (1981), and McFarlane (1987). Nonorographic waves are triggered by two mechanisms in CAM5: convective heating rates which are calculated diagnostically and a frontogenesis function from Hoskins (1982). Orographic waves are produced following McFarlane (1987). These parameterizations are only effective for large-scale wave activity, however. The subgrid scale of high-frequency gravity waves, such as those found in the TTL, makes GCMs ill equipped to resolve them (e.g., Dean et al., 2005). Furthermore, reanalysis data can resolve longer period waves but cannot resolve short period waves found in the TTL (Kim & Alexander, 2013, 2015).

To test how these waves might affect the performance of the model, two random temperature perturbations were applied to the simulated TTL every time step (30 min). Kim et al. (2016) used ATTREX 3 aircraft observations to show that wave activity impacted TWP TTL temperatures by as much as 5 K with a majority of the temperature anomalies lying between −2.2 and 2.2 K. We use this same temperature range for one of the random temperature perturbation simulations (RW2.2K hereafter). The other simulation uses a 1-K temperature anomaly (RW1K hereafter) in order to show how a subtler temperature anomaly range may impact TTL clouds. The 1-K value was chosen because it is more representative of findings from previous TTL wave anomaly studies which used radiosondes (e.g., Kim & Alexander, 2015). Each of these random temperature perturbations was applied to the CF1-2K simulation. Unfortunately, in this crude parameterization, there is no horizontal coherence to these random temperature perturbations. Regardless, including the random temperature perturbations every time step should act as a first order approximation of a high-frequency gravity wave and show the potential impact upon TTL cirrus in the simulations. The impact upon the simulated extinction distribution is represented by the turquoise and purple lines in Figure 13b. The inclusion of a 1-K random temperature fluctuation (turquoise line) has little impact on CF1-2K extinction frequency except at extinction values larger than 0.7 km^{-1}, which are no longer are present. The RW2.2K simulation (purple line) shows an increase in the frequency of small extinction values (< 0.02 km^{-1}) relative to the CF1-2K simulation in Figure 9. Those small extinction values now exceed CAL-LV2 and H-2DS observations by as much as a factor of 2. The inclusion of 2.2-K random gravity waves has decreased the large extinction event boundary in the CF1-2K case from 1 km^{-1} in Figure 9 to 0.2 km^{-1} in Figure 13b as well.

Further impacts from the random gravity wave simulations upon cloud fraction, RHi, and water vapor mixing ratio are shown in Figure 14. The cloud frequency along the flight track (Figure 14a) responds to a 1-K wave stimulus with a 10% increase in clear sky conditions compared to the CF1-2K case. No change in full cloud cover occurred. Instead, there are fewer instances of partly cloudy conditions. The 2.2-K wave stimulus caused instances of full cloud cover to increase by 7% from the CF1-2K case and now lies within 4% of the cloud probe observations. Clear-sky instances in the RW2.2K case have been reduced by 4% in response to the increase in clouds.

The cloud fraction curtain for the RW2.2K simulation is shown in Figure 14b. There are consistent cloud fractions of 0.9 between 16 and 18 km throughout most of the flight. The RW2.2K simulation also produced more clouds within the timeframe when the Global Hawk encountered convection (10–13 hr) than in the CF1-2K case.

In Figure 14c the magnitude of the RHi peak of the RW1K case has broadened relative to CF1-2K case and now covers the 60–100% RHi range. Approximately 61% of the simulated RHi falls within this range. The RW1K more closely resembles the CAM5/CARMA case. The RW2.2K distribution is much narrower than

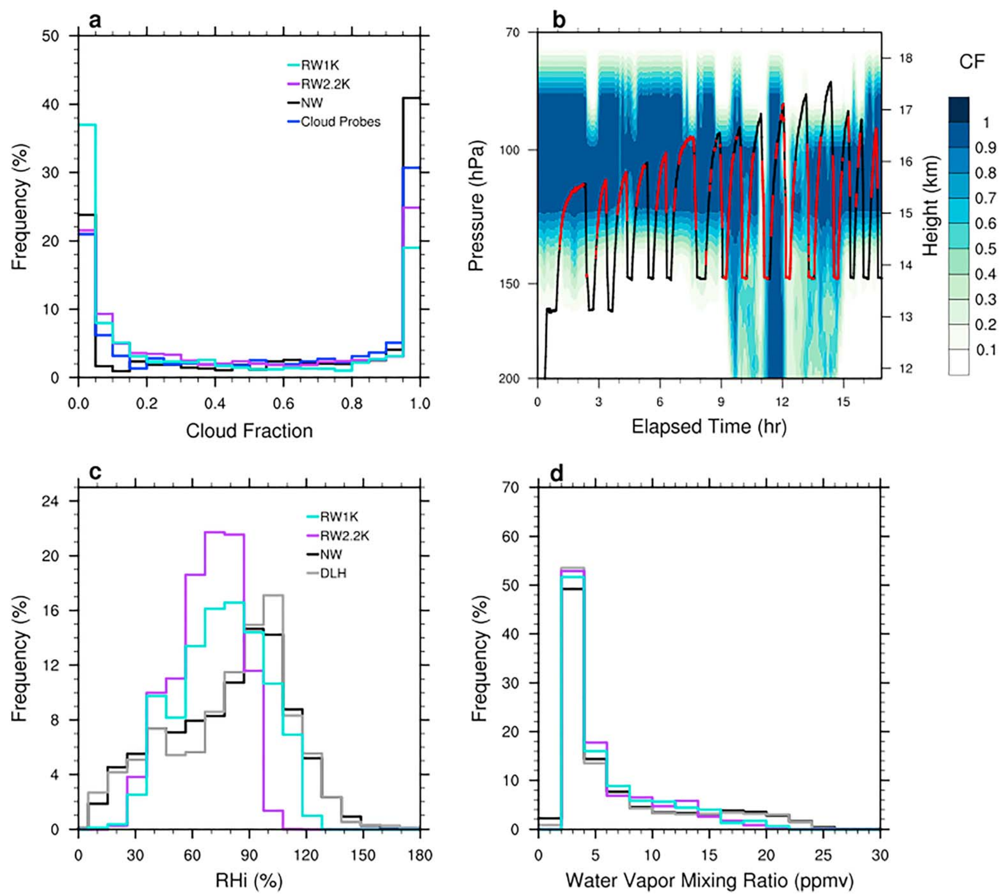

Figure 14. Same as Figure 4 but for the random gravity wave simulations. The cloud fraction curtain in panel (b) is from the RW2.2K case. CF = cloud fraction; NW = National Oceanic and Atmospheric Administration Water.

all other simulations and is centered around a lower RHi of 70–80%. The water vapor distributions from the wave cases (Figure 14d) show only small differences compared to the CF1-2K case from Figure 6d, which is not unexpected due vapor mass being relatively insensitive to temperature.

The introduction of random temperature perturbations has increased the number of ice crystals smaller than 10 μm in size by as much as half of an order of magnitude in both cases (Figure 15). In fact, the simulated concentration of ice crystals smaller than 10 μm (5 μm) in size exceeds the upper limit of the observational spread in the RW2.2K (RW1K) case. Elsewhere, the RW1K case's number distribution resembles the in situ ice distribution produced by the CF1-2K case from Figure 5. The RW2.2K case generally produces more ice crystals smaller than 100 μm than shown by the CF1-2K case's total ice concentration (in situ + detrained ice). Larger ice crystals remain relatively unchanged except for a small reduction in the large particle tail. The mass distribution of RW1K again more closely resembles the CF1-2K in situ ice case (Figure 5) except for particles smaller than 5 μm where there is an order of magnitude increase (Figure 15). The RW2.2K case's mass distribution has a similar shape and magnitude to the CF1-2K total ice mass distribution.

Figures 13b, 14, and 15 likely reveal the limitations of the random gravity wave parameterization utilized in this study. The first-order approximation succeeds at creating more small ice crystals (Figure 15) and cirrus clouds (Figures 14a and 14c) as the literature would suggest. However, both of the random temperature perturbations shifted the simulated TTL RHi to lower values (Figure 14b), which disagrees with previous work. This dehydration likely results from the lack of temporal and horizontal coherence in the parameterization. Without proper temporal and horizontal coherence, the sublimation/evaporation associated with the warming phase of a propagating wave does not always occur at the correct time or magnitude. As a result, the high ice crystal numbers created are allowed to persist within cloud, which completely dehydrates the simulated

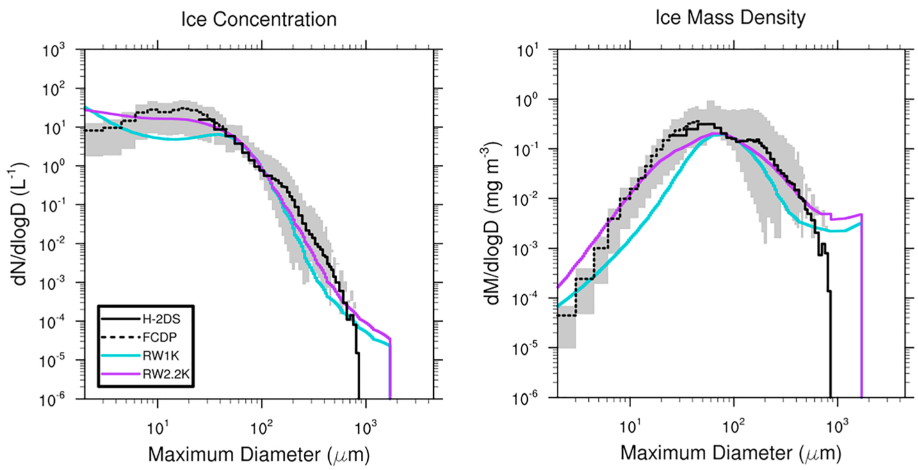

Figure 15. Same as Figure 7 but for the RW2.2K (purple) and RW1K (turquoise) random gravity wave simulations. Only total ice concentration and mass are shown for the simulations.

TTL. Furthermore, the wave period used here (30 min) is on the high-frequency end of possible TTL wave spectrums. The simulated clouds may not have enough time to completely evolve from one temperature perturbation prior to being clobbered by a new, unrelated temperature stimulus. One would expect with more small ice crystals, in-cloud extinction would increase, however, that is not the case as shown by Figure 13b. The answer to this problem lies in the cloud fraction curtain of Figure 14b. While there is an increase in the population of small ice crystals, the crystals are spread out over a larger area, and thus not actually creating more optically thick clouds.

From the simple gravity wave test performed here it is difficult to discern if their inclusion will greatly improve the overall representation of TTL cirrus within the CAM5/CARMA model. However, we do note impacts to TTL ice crystal number and cloud frequency which are in agreement with previous studies (Hoyle et al., 2005; E. Jensen & Pfister, 2004; Kärcher & Lohmann, 2002; Kärcher & Ström, 2003; M. R. Schoeberl et al., 2015; Ueyama et al., 2015). A more comprehensive gravity wave parameterization is needed to provide a more diffinitive answer. While such a parameterization is still likely beyond the abilities of CAM5 without substantial changes to the model, a further improvement to the wave parameterization presented in this study could be done by including a time dependent wave equation, which takes into account wave stimulation and damping over the course of multiple simulation time steps. The implementation of such a modification should also consider the incorporation of waves of varying frequency. Previous model studies have also shown the necessity of considering both high-frequency and low-frequency waves in producing improved ice nucleation rates and particle concentrations (e.g., Jensen, Ueyama, et al., 2016; Spichtinger & Krämer, 2013). These improved ice nucleation rates would help to further address the dry cloud layers exhibited by the CAM5/CARMA simulation. The subsequent larger nucleation rates would lead to the formation of numerous small ice crystals and prevent large ice crystals, which sediment out quickly and irreversibly dry the cloud layer, from forming.

Regardless of the gravity waves, this study has concluded that while Bardeen et al. (2013) showed the abilities of CARMA to improve the global representation of ice clouds within Community Earth System Model, the subgrid parameterization for cloud fraction and supersaturation made in CARMA are not sufficient for TTL cirrus. Grid box-scale assumptions are required instead. Furthermore, vertical resolution remains an issue in the simulated TTL. The modifications presented in this study significantly improved TTL cirrus cloud fraction and RHi. However, it is important to note that these are only temporary fixes.

5. Summary and Future Work

This study has provided insight into the performance of the CAM5/CARMA model for TTL cirrus clouds. Bardeen et al. (2013) showed that CAM5/CARMA improves upon the global representation of ice clouds relative to the Morrison and Gettelman (2008) cloud scheme. This study expanded upon Bardeen et al.'s

(2013) findings by focusing attention on TTL cirrus clouds backed up by a robust data set of observations from the ATTREX 3 field mission and the CALIPSO satellite mission. Simulations show that the CAM5/CARMA model and the CAM5/MG model underrepresented TTL cirrus fraction along the ATTREX 3 flight track. This was due to the fact that the Wilson and Ballard (1999) cloud scheme used in CAM5/CARMA is more suited for middle-to-lower troposphere clouds where convection is important and cloud extent is smaller than the size of a GCM grid box. In response, two adjustments were implemented. First, tropical cloud fraction was set to one and the grid box RH was used whenever cloud was present for altitudes at or above 120 hPa. The model tropopause temperatures were also lowered by 2 K in the tropics to account for the poor model resolution of the cold point tropopause. The results of said modifications increased the frequency of full cloud cover simulated along the ATTREX 3 flight track and improved RH. These modifications also improved the in-cloud size and mass distributions for particles smaller than 100 μm in size and showed that when in situ ice created by CARMA was the dominant ice type, the model performed better than when ice was provided by parameterizations of detrained ice from convective clouds. Between the two modifications, the change to the diagnosis of cloud fraction proved to be the most important factor for improving simulated TTL cirrus.

An issue with detrained ice from CAM5, which caused CARMA to create detrained ice particles in its largest size bins, was also noted. It is possible these particles exist in nature and are simply so rare that they are not observed with current instruments. Sampling bias could have also played a role in the lack of observations of these particles. However, the large particles may also be an artifact of the treatment of detrained ice.

Simulated TTL cloud extinction was evaluated with both aircraft and satellite observations, and it was found that all simulations produced too few instances of large extinction. The default CAM5/CARMA and the modified CF1-2K simulations had too few small extinction values while the CAM5/MG case had too many instances. The removal of convectively influenced observations from the H-2DS data set improved the agreement between observations and the CF1-2K simulation, but overall comparisons were still poor. The introduction of a modest random temperature perturbations to the CF1-2K case increased the amount of small extinction values and decreased large extinction values. Evaluations of in-cloud ice concentration and mass, RHi, and cloud fraction produced by the random gravity wave simulation revealed that the lack of a time dependent wave equation and horizontal coherence prevented the parameterization from properly removing ice, which formed during the cooling phase of a wave. A more comprehensive gravity wave parameterization than the one presented in this study may further improve the extinction issue. An improved representation of convection might also account for the lack of high extinction values.

In order to ensure that the CF1-2K simulation kept CAM5/CARMA in radiative balance, an investigation of the impact these model modifications had upon simulated global cloud fraction and LWCF was performed. This analysis yielded results that suggested the CF1-2K modifications produced less cloud longwave forcing than CAM5/MG but has a nearly identical LWCF to CAM5/CARMA. All model variants are biased low compared with Clouds and the Earth's Radiant Energy System's Energy Balance and Filled observations. These low forcings may result from poor vertical resolution or reflect the inability of the model to produce clouds with high extinctions, which in turn may require a better model of gravity waves.

Lastly, we recommend a number of avenues for further CAM5 and CARMA model development, which could provide more realistic cirrus cloud representation.

1. One inherent limitation of how CAM5 and CARMA relate cloud fraction and RH is their inability to resolve small-scale variability caused by subgrid-scale fluctuations in temperature, absolute humidity, and updraft velocities. A statistical approach to cloud fraction would provide the subgrid information needed to better represent cirrus (e.g., Kärcher & Burkhardt, 2008). Furthermore, using a statistical scheme to predict the subgrid water content variability would provide CAM5/CARMA with the agency to simulate either large-scale optically thin clouds or small-scale optically thick clouds connected with the same IWC. We should note, however, the results from this study show that assumptions for modeling TTL cirrus should differ from those made for cirrus in the free troposphere. Subgrid variability is less important for TTL clouds that possess horizontal coverage approaching grid box resolution. At these horizontal extents, the grid box average values should suffice, though the coarse vertical resolution remains a problem. A future PDF scheme should look to incorporate a family of PDFs, which can account for the subgrid variability of the free troposphere, yet expand to use grid box-scale values in the TTL.

2. Only briefly mentioned in this study, but a more comprehensive representation of ice nucleation within the TTL is needed. Currently, CARMA only performs homogeneous nucleation, but more recent work has suggested that heterogeneous nucleation may play a larger role in the TTL than previously thought (Jensen et al., 2018). Changing CARMA to have interactive sulfates which update the local ambient sulfate populations when ice nucleates is one fix. Furthermore, the inclusion of heterogeneous nucleation may improve cirrus ice microphysics, as well as provide insight into the role of heterogeneous nucleation within the TTL.
3. A more realistic gravity wave parameterization could improve CAM5/CARMA TTL ice concentrations, cloud frequency, and moisture. Such a parameterization would need to consider waves of varying frequency and include a time dependent wave equation.
4. Improved horizontal and vertical resolution of GCM grid boxes will lessen the need for cloud fraction schemes as physical processes can be explicitly treated.

Acknowledgments
This work was supported in by NASA Award NNX14AR56G Atmospheric Composition Campaign Data Analysis and Modeling Program and the NSF Climate and Large-Scale Dynamics Program AGS1640903 Grant. The ATTREX 3 data used in this study are open to the public and can be found on the NASA Earth Science Project website (espoarchive.nasa.gov). The authors would also like to express gratitude for all of the hard work done by the instrument teams involved in ATTREX, as well as the CALIPSO and CALIPSO-GOCCP teams. The CALIPSO Level 2 and CERES-EBAF data used in this study were obtained from the NASA Langley Research Center Atmospheric Science Data Center (eosweb.larc.nasa.gov). CALIPSO-GOCCP data are freely available and can be found on the ClimServ CFMIP web page (climserv.ipsl.polytechnique.fr/cfmip-obs). The CPL data used in this study are open to the public and can be found at the Cloud Physics Lidar homepage (https://cpl.gsfc.nasa.gov). Special thanks to Melody Avery, Jennifer Kay, and Matthew McGill for their guidance on how to use the CALIPSO, CALIPSO-GOCCP, and CPL data. We would like to acknowledge high-performance computing support from Cheyenne (doi:10.5065/D6RX99HX) provided by NCAR's Computational and Information Systems Laboratory, sponsored by the National Science Foundation. All simulation output used in this study can be found online (doi: osf.io/3ake6).

References

Anthes, R. A., Bernhardt, P. A., Chen, Y., Cucurull, L., Dymond, K. F., Ector, D., et al. (2008). The cosmic/formosat-3 mission: Early Results. *Bulletin of the American Meteorological Society*, *3*.

Avery, M., Winker, D., Heymsfield, A., Vaughan, M., Young, S., Hu, Y., & Trepte, C. (2012). Cloud ice water content retrieved from the CALIOP space-based lidar. *Geophysical Research Letters*, *39*, L05808. http://doi.org/10.1029/2011GL050545

Bardeen, C. G., Gettelman, A., Jensen, E. J., Heymsfield, A., Conley, A. J., Delanoë, J., et al. (2013). Improved cirrus simulations in a general circulation model using CARMA sectional microphysics. *Journal of Geophysical Research: Atmospheres*, *118*, 11,679–11,697. http://doi.org/10.1002/2013JD020193

Bardeen, C. G., Toon, O. B., Jensen, E. J., Marsh, D. R., & Harvey, V. L. (2008). Numerical simulations of the three-dimensional distribution of meteoric dust in the mesosphere and upper stratosphere. *Journal of Geophysical Research*, *113*(D17). http://doi.org/10.1029/2007JD009515

Bergman, J. W., Jensen, E. J., Pfister, L., & Bui, T. V. (2016). Air parcel trajectory dispersion near the tropical tropopause. *Journal of Geophysical Research: Atmospheres*, *121*, 3759–3775. http://doi.org/10.1002/2015JD024320.Received

Bergman, J. W., Jensen, E. J., Pfister, L., & Yang, Q. (2012). Seasonal differences of vertical-transport efficiency in the tropical tropopause layer: On the interplay between tropical deep convection, large-scale vertical ascent, and horizontal circulations. *Journal of Geophysical Research*, *117*(D5), 1–20. http://doi.org/10.1029/2011JD016992

Bodas-Salcedo, A., Webb, M. J., Bony, S., Chepfer, H., Durfresne, J. L., Klein, S. A., et al. (2011). COSP: Satellite simulation software for model assessment. *Bulletin of the American Meteorological Society*, *92*(8), 1023–1043. http://doi.org/10.1175/2011BAMS2856.1

Chepfer, H., Bony, S., Winker, D., Cesana, G., Dufresne, J. L., Minnis, P., et al. (2010). The GCM-oriented CALIPSO cloud product (CALIPSO-GOCCP). *Journal of Geophysical Research-Atmospheres*, *115*(5). http://doi.org/10.1029/2009JD012251

Colella, P., & Woodward, P. R. (1984). The piecewise parabolic method (PPM) for gas-dynamical simulations. *Journal of Computational Physics*, *54*(1), 174–201. http://doi.org/10.1016/0021-9991(84)90143-8

Comstock, J. M., Ackerman, T. P., & Mace, G. G. (2002). Ground-based lidar and radar remote sensing of tropical cirrus clouds at Nauru Island: Cloud statistics and radiative impacts. *Journal of Geophysical Research*, *107*(D23), AAC 16-1–AAC 16-14. http://doi.org/10.1029/2002JD002203

Corti, T., Luo, B. P., Fu, Q., Vömel, H., & Peter, T. (2006). The impact of cirrus clouds on tropical troposphere-to-stratosphere transport. *Atmospheric Chemistry and Physics*, *6*(2), 1725–1747. http://doi.org/10.5194/acpd-6-1725-2006

Cziczo, D. J., Froyd, K. D., Hoose, C., Jensen, E. J., Diao, M., Zondlo, M. A., et al. (2013). Clarifying the dominant sources and mechanisms of cirrus cloud formation. *Science*, *340*(6138), 1320–1324. http://doi.org/10.1126/science.1234145

Davis, S., Hlavka, D., Jensen, E., Rosenlof, K., Yang, Q., Schmidt, S., et al. (2010). In situ and lidar observations of tropopause subvisible cirrus clouds during TC4. *Journal of Geophysical Research*, *115*, 115. http://doi.org/10.1029/2009JD013093

Dean, S., Lawrence, B. N., & Grainger, R. G. (2005). Orographic cloud in a GCM: The missing cirrus. *Climate Dynamics*, *24*(7-8), 771–780. http://doi.org/10.1007/s00382-005-0020-9

Delanoë, J., & Hogan, R. J. (2008). A variational scheme for retrieving ice cloud properties from combined radar, lidar, and infrared radiometer. *Journal of Geophysical Research*, *113*(D7). http://doi.org/10.1029/2007JD009000

Delanoë, J., & Hogan, R. J. (2010). Combined CloudSat-CALIPSO-MODIS retrievals of the properties of ice clouds. *Journal of Geophysical Research*, *115*. http://doi.org/10.1029/2009JD012346

Deng, M., Mace, G. G., Wang, Z., & Okamoto, H. (2010). Tropical Composition, Cloud and Climate Coupling Experiment validation for cirrus cloud profiling retrieval using CloudSat radar and CALIPSO lidar. *Journal of Geophysical Research*, *115*. http://doi.org/10.1029/2009JD013104

Diskin, G. S., Podolske, J. R., Sachse, G. W., & Slate, T. A. (2002). Open-path airborne tunable diode laser hygrometer. *International Symposium on Optical Science and Technology*, *4817*, 196–204. http://doi.org/10.1117/12.453736

English, J. M., Toon, O. B., Mills, M. J., & Yu, F. (2011). Microphysical simulations of new particle formation in the upper troposphere and lower stratosphere. *Atmospheric Chemistry and Physics*, *11*(17), 9303–9322. http://doi.org/10.5194/acp-11-9303-2011

Froyd, K. D., Murphy, D. M., Lawson, P., Baumgardner, D., & Herman, R. L. (2010). Aerosols that form subvisible cirrus at the tropical tropopause. *Atmospheric Chemistry and Physics*, *10*(1), 209–218. https://doi.org/10.5194/acp-10-209-2010

Fueglistaler, S., Dessler, A. E., Dunkerton, T. J., Folkins, I., Fu, Q., & Mote, P. W. (2009). Tropical tropopause layer. *Reviews of Geophysics*, *47*, RG1004. http://doi.org/10.1029/2008RG000267

Garcia, R. R., & Solomon, S. (1985). The effect of breaking gravity waves on the dynamics and chemical composition of the mesosphere and lower thermosphere. *Journal of Geophysical Research*, *90*(D2), 3850–3868. https://doi.org/10.1029/JD090iD02p03850

Getzewich, B., Tackett, J. L., Kar, J., Garnier, A., Vaughan, M. A., & Hunt, B. (2016). CALIOP calibration: Version 4.0 algorithm updates. *EPJ Web of Conferences*, *119*, 8–11. http://doi.org/10.1051/epjconf/201611904013

Haladay, T., & Stephens, G. (2009). Characteristics of tropical thin cirrus clouds deduced from joint CloudSat and CALIPSO observations. *Journal of Geophysical Research*, *114*, 114. http://doi.org/10.1029/2008JD010675

Heymsfield, A. J. (1986). Ice particles observed in a cirriform cloud at −83 °C and implications for polar stratospheric clouds. *Journal of Atmospheric Science*, *43*(8), 851–855. https://doi.org/10.1175/1520-0469(1986)043<0851:IPOIAC>2.0.CO;2

Heymsfield, A. J., Schmitt, C., Bansemer, A., & Twohy, C. H. (2010). Improved representation of ice particle masses based on observations in natural clouds. *Journal of the Atmospheric Sciences*, *67*(10), 3303–3318. http://doi.org/10.1175/2010JAS3507.1

Holton, J. R. (1982). The role of gravity wave induced drag and diffusion in the momentum budget of the mesosphere. *Journal of the Atmospheric Sciences*, *39*(4), 791–799. https://doi.org/10.1175/1520-0469(1982)039<0791:TROGWI>2.0.CO;2

Hong, G. (2007). Parameterization of scattering and absorption properties of nonspherical ice crystals at microwave frequencies. *Journal of Geophysical Research*, *112*, D11208. http://doi.org/10.1029/2006JD008364

Hoose, C., & Möhler, O. (2012). Heterogeneous ice nucleation on atmospheric aerosols: A review of results from laboratory experiments. *Atmospheric Chemistry and Physics*, *12*(20), 9817–9854. http://doi.org/10.5194/acp-12-9817-2012

Hoskins, B. J. (1982). The mathematical theory of frontogenesis. *Annual Review of Fluid Mechanics*, *14*(1), 131–151. http://doi.org/10.1146/annurev.fl.14.010182.001023

Hoyle, C. R., Luo, B. P., & Peter, T. (2005). The origin of high ice crystal number densities in cirrus clouds. *Journal of the Atmospheric Sciences*, *62*(7), 2568–2579. https://doi.org/10.1175/JAS3487.1

Jensen, E., & Pfister, L. (2004). Transport and freeze-drying in the tropical tropopause layer. *Journal of Geophysical Research*, *109*(D2). http://doi.org/10.1029/2003JD004022

Jensen, E. J., Kärcher, B., Ueyama, R., Pfister, L., Bui, T. V., Diskin, G. S., et al. (2018). Heterogeneous ice nucleation in the tropical tropopause layer. *Journal of Geophysical Research: Atmospheres*, *123*(21), 12,210–12,227. http://doi.org/10.1029/2018JD028949

Jensen, E. J., Pfister, L., & Bui, T. P. (2012). Physical processes controlling ice concentrations in cold cirrus near the tropical tropopause. *Journal of Geophysical Research*, *117*(D11), 1–9. http://doi.org/10.1029/2011JD017319

Jensen, E. J., Pfister, L., Bui, T.-P., Lawson, P., & Baumgardner, D. (2010). Ice nucleation and cloud microphysical properties in tropical tropopause layer cirrus. *Atmospheric Chemistry and Physics*, *9*(5), 20,631–20,675. http://doi.org/10.5194/acpd-9-20631-2009

Jensen, E. J., Pfister, L., Jordan, D. E., Bui, T. V., Ueyama, R., Singh, H. B., et al. (2016). The NASA Airborne Tropical TRopopause EXperiment (ATTREX): High-altitude aircraft measurements in the tropical western Pacific. Bulletin of the American Meteorological Society. http://doi.org/10.1175/BAMS-D-14-00263.1, *98*, 1, 129, 143

Jensen, E. J., Toon, O. B., Pfister, L., & Selkirk, H. B. (1996). Dehydration of the upper troposphere and lower stratosphere by subvisible cirrus clouds near the tropical tropopause. *Geophysical Research Letters*, *23*(8), 825–828. http://doi.org/10.1029/96GL00722

Jensen, E. J., Ueyama, R., Pfister, L., Bui, T.-P., Lawson, R. P., Woods, S., et al. (2016). On the susceptibility of cold tropical cirrus to ice nuclei abundance. *Journal of the Atmospheric Sciences*, *73*(6), 2445–2464. http://doi.org/10.1175/JAS-D-15-0274.1

Jensen, E. J., Ueyama, R., Pfister, L., Bui, T. V., Alexander, M. J., Podglajen, A., et al. (2016). High-frequency gravity waves and homogeneous ice nucleation in tropical tropopause layer cirrus. *Geophysical Research Letters*, *43*, 6629–6635. http://doi.org/10.1002/2016GL069426

Jiang, J. H., Su, H., Zhai, C., Perun, V. S., Del Genio, A., Nazarenko, L. S., et al. (2012). Evaluation of cloud and water vapor simulations in CMIP5 climate models Using NASA "A-Train" satellite observations. *Journal of Geophysical Research*, *117*(D14). http://doi.org/10.1029/2011JD017237

Kärcher, B., & Burkhardt, U. (2008). A cirrus cloud scheme for general circulation models. *Quarterly Journal of the Royal Meteorological Society*, *134*(635), 1439–1461. http://doi.org/10.1002/qj

Kärcher, B., & Lohmann, U. (2002). A parameterization of cirrus cloud formation: Homogeneous freezing of supercooled aerosols. *Journal of Geophysical Research*, 107.

Kärcher, B., & Ström, J. (2003). The roles of dynamical variability and aerosols in cirrus cloud formation. *Atmospheric Chemistry and Physics*, *3*(3), 823–838. https://doi.org/10.5194/acp-3-823-2003

Kay, J. E., Hillman, B. R., Klein, S. A., Zhang, Y., Medeiros, B., Pincus, R., et al. (2012). Exposing global cloud biases in the Community Atmosphere Model (CAM) using satellite observations and their corresponding instrument simulators. *Journal of Climate*, *25*(15), 5190–5207. http://doi.org/10.1175/JCLI-D-11-00469.1

Kim, J., & Alexander, M. J. (2013). A new wave scheme for trajectory simulations of stratospheric water vapor. *Geophysical Research Letters*, *40*, 5286–5290. http://doi.org/10.1002/grl.50963

Kim, J., & Alexander, M. J. (2015). Direct impacts of waves on tropical cold point tropopause temperature. *Geophysical Research Letters*, *42*, 1584–1592. http://doi.org/10.1002/2014GL062737

Kim, J., Alexander, M. J., Bui, T. P., Dean-Day, J. M., Lawson, R. P., Woods, S., et al. (2016). Ubiquitous influence of waves on tropical high cirrus clouds. *Geophysical Research Letters*, *43*, 5895–5901. http://doi.org/10.1002/2016GL069293.Received

Koop, T., Luo, B., Tsias, A., & Peter, T. (2000). Water activity as the determinant for homogeneous ice nucleation in aqueous solutions. *Nature*, *406*(6796), 611–614. https://doi.org/10.1038/35020537

Korolev, A., & Issac, G. (2003). Roundness and aspect ratio of particles in ice clouds. *Journal of Atmospheric Science*, *60*(15), 1795–1808. https://doi.org/10.1175/1520-0469(2003)060<1795:RAAROP>2.0.CO;2

Lamarque, J. F., Emmons, L. K., Hess, P. G., Kinnison, D. E., Tilmes, S., Vitt, F., et al. (2011). CAM-chem: description and evaluation of interactive atmospheric chemistry in the Community Earth System Model. *Geoscientific Model Development*, *5*(2), 369–411. http://doi.org/10.5194/gmd-5-369-2012

Lawson, P., Gurganus, C., & Woods, S. (2017). Aircraft observations of cumulus microphysics ranging from the tropics to midlatitudes: Implications for a '"new" secondary ice process. *Journal of Atmospheric Science*, *74*(9), 2899–2920. http://doi.org/10.1175/JAS-D-17-0033.1

Lawson, R. P., Baker, B. A., & Schmitt, C. G. (2001). An overview of microphysical properties of Arctic clouds observed in May and July 1998 during FIRE ACE. *Journal of Geophysical Research*, *106*(D14), 14,989–15,014. http://doi.org/https://doi.org/10.1029/2000JD900789

Lawson, R. P., O'Connor, D., Zmarzly, P., Weaver, K., Baker, B., Mo, Q., & Jonsson, H. (2006). The 2D-S (stereo) probe: Design and preliminary tests of a new airborne, high-speed, high-resolution particle imaging probe. *Journal of Atmospheric and Oceanic Technology*, *23*(11), 1462–1477. http://doi.org/10.1175/JTECH1927.1

Lawson, R. P., Pilson, B., Baker, B., Mo, Q., Jensen, E., Pfister, L., & Bui, P. (2008). Aircraft measurements of microphysical properties of subvisible cirrus in the tropical tropopause layer. *Atmospheric Chemistry and Physics*, *7*(3), 6255–6292. http://doi.org/10.5194/acpd-7-6255-2007

Lindzen, R. S. (1981). Turbulence and stress owing to gravity wave and tidal breakdown. *Journal of Geophysical Research*, *86*(C10), 9707–9714. https://doi.org/10.1029/JC086iC10p09707

Liu, X., Easter, R. C., Ghan, S. J., Zaveri, R., Rasch, P., Shi, X., et al. (2012). Toward a minimal representation of aerosols in climate models: Description and evaluation in the Community Atmosphere Model CAM5. *Geoscientific Model Development*, *5*(3), 709–739. http://doi.org/10.5194/gmd-5-709-2012

Liu, X., & Penner, J. E. (2005). Ice nucleation parameterization for global models. *Meteorologische Zeitschrift*, *14*(4), 499–514. http://doi.org/10.1127/0941-2948/2005/0059

Liu, X., Penner, J. E., Ghan, S. J., & Wang, M. (2007). Inclusion of ice microphysics in the NCAR Community Atmospheric Model Version 3 (CAM3). *Journal of Climate*, *20*(18), 4526–4547. http://doi.org/10.1175/JCLI4264.1

Loeb, N. G., Doelling, D. R., Wang, H., Su, W., Nguyen, C., Corbett, J. G., et al. (2018). Clouds and the Earth's Radiant Energy System (CERES) Energy Balanced and Filled (EBAF) Top-of-Atmosphere (TOA) Edition-4.0 Data Product. *Journal of Climate*, *31*(2), 895–918. https://doi.org/10.1175/jcli-d-17-0208.1

Massie, S. T., Gille, J., Craig, C., Khosravi, R., Barnett, J., Read, W., & Winker, D. (2010). HIRDLS and CALIPSO observations of tropical cirrus. *Journal of Geophysical Research*, *115*, 1–15. http://doi.org/10.1029/2009JD012100

McFarlane, N. A. (1987). The effect of orographically excited gravity wave drag on the general circulation of the lower stratosphere and troposphere. *Journal of the Atmospheric Sciences*, *44*(14), 1775–1800. https://doi.org/10.1175/1520-0469(1987)044<1775:TEOOEG>2.0.CO;2

McGill, M., Hlavka, D., Hart, W., Scott, V. S., Spinhirne, J., & Schmid, B. (2002). Cloud physics lidar: Instrument description and initial measurement results. *Applied Optics*, *41*(18), 3725–3734. http://doi.org/10.1364/AO.41.003725

Molod, A., Takacs, L., Suarez, M., & Bacmeister, J. (2015). Development of the GEOS-5 atmospheric general circulation model: Evolution from MERRA to MERRA2. *Geoscientific Model Development*, *8*(5), 1339–1356. http://doi.org/10.5194/gmd-8-1339-2015

Morrison, H., & Gettelman, A. (2008). A new two-moment bulk stratiform cloud microphysics scheme in the Community Atmosphere Model, Version 3 (CAM3). Part I: Description and numerical tests. *Journal of Climate*, *21*(15), 3642–3659. http://doi.org/10.1175/2008JCLI2105.1

Murray, B. J., Salzmann, C. G., Heymsfield, A. J., Dobbie, S., Neely, R. R., & Cox, C. J. (2015). Trigonal ice crystals in Earth's atmosphere. *Bulletin of the American Meteorological Society*, *96*(9) (September)), 1519–1531. http://doi.org/10.1175/BAMS-D-13-00128.1

Pfister, L., Selkirk, H. B., Jensen, E. J., Schoeberl, M. R., Toon, O. B., Browell, E. V., et al. (2001). Aircraft observations of thin cirrus clouds near the tropical tropopause. *Journal of Geophysical Research*, *106*(D9), 9765–9786. http://doi.org/10.1029/2000JD900648

Podglajen, A., Plougonven, R., Hertzog, A., & Jensen, E. (2018). Impact of gravity waves on the motion and distribution of atmospheric ice particles. *Atmospheric Chemistry and Physics*, *18*(14), 10,799–10,823. https://doi.org/10.5194/acp-18-10799-2018

Pruppacher, H. R., Klett, J. D., & Springer (1997). *Microphysics of clouds and precipitation*. Kluwer Academic Publishers. Retrieved from https://books.google.com/books?id=Nk40jwEACAAJ

Ramanathan, V., Cess, R. D., Harrison, E. F., Minnis, P., Barkstrom, B. R., Ahmadr, E., & Hartmann, D. (1989). Cloud-radiative forcing and climate: Results from the Earth Radiation Budget Experiment. *Science*, *243*(4887), 57–63. http://doi.org/10.1126/science.243.4887.57

Randel, W. J., & Jensen, E. J. (2013). Physical processes in the tropical tropopause layer and their roels in a changing climate. *Nature Geoscience*, *6*(3), 169–176. http://doi.org/10.1038/ngeo1733

Rocken, C., Kuo, Y., Schreiner, W., Hunt, D., Sokolovskiy, S., & Mccormick, C. (2000). COSMIC System Description. *Terrestrial, Atmospheric and Oceanic Sciences*, *11*(1), 021–052. https://doi.org/10.3319/TAO.2000.11.1.21(COSMIC)

Rossow, W. B., & Schiffer, R. A. (1999). Advances in understanding clouds from ISCCP. *Bulletin of the American Meteorological Society*, *80*(11), 2261–2287. http://doi.org/10.1175/1520-0477(1999)080<2261:AIUCFI>2.0.CO;2

Sassen, K., & Cho, B. S. (1992). Subvisual-thin cirrus lidar dataset for satellite verification and climatological research. *American Meteorological Society*, *31*, 1275–1285. http://doi.org/10.1175/1520-0450(1992)031<1275:STCLDF>2.0.CO;2

Schoeberl, M., Dessler, A., Ye, H., Wang, T., Avery, M., & Jensen, E. (2016). The impact of gravity waves and cloud nucleation threshold on stratospheric water and tropical tropospheric cloud fraction. *Earth and Space Science*, *3*, 295–305. http://doi.org/10.1002/2016EA000180

Schoeberl, M. R., Dessler, A. E., Wang, T., Avery, M. A., & Jensen, E. J. (2014). Cloud formation, convection, and stratospheric dehydration. *Earth and Space Science*, *1*, 1–17. http://doi.org/10.1002/2014EA000014.Received

Schoeberl, M. R., Jensen, E. J., & Woods, S. (2015). Gravity waves amplify upper tropospheric dehydration by clouds. *Earth and Space Science*, *2*, 485–500. http://doi.org/10.1002/2015EA000127.Received

Slingo, J. M. (1987). The development and verification of a cloud prediction scheme for the ECMWF model. *Quarterly Journal of the Royal Meteorological Society*, *113*(477), 899–927. https://doi.org/10.1002/qj.49711347710

Spichtinger, P., & Krämer, M. (2013). Tropical tropopause ice clouds: A dynamic approach to the mystery of low crystal numbers. *Atmospheric Chemistry and Physics*, *13*(19), 9801–9818. http://doi.org/10.5194/acp-13-9801-2013

Thornberry, T. D., Rollins, A. W., Gao, R. S., Watts, L. A., Ciciora, S. J., Mclaughlin, R. J., & Fahey, D. W. (2015). A two-channel, tunable diode laser-based hygrometer for measurement of water vapor and cirrus cloud ice water content in the upper troposphere and lower stratosphere. *Atmospheric Measurement Techniques*, *8*(1), 211–224. http://doi.org/10.5194/amt-8-211-2015

Toon, O. B., Turco, R. P., Westphal, D., Malone, R., & Liu, M. S. (1988). A multidimensional model for aerosols: Description of computational analogs. *American Meteorological Society*, *45*(15), 2123–2144. http://doi.org/https://doi.org/10.1175/1520-0469(1988)045<2123:AMMFAD>2.0.CO;2

Turco, R. P., Hamill, P., Toon, O. B., Whitten, R. C., & Kiang, C. S. (1979). A one-dimensional model describing aerosol formation and evolution in the stratosphere: I. Physical Processes and Mathematical Analogs. *American Meteorological Society*, *36*, 699–717.

Ueyama, R., Jensen, E. J., Pfister, L., & Kim, J. (2015). Dynamical, convective, and microphysical control on wintertime distributions of water vapor and clouds in the tropical tropopause layer. *Journal of Geophysical Research: Atmospheres*, *120*, 10,483–10,500. http://doi.org/10.1002/2015JD023318.Received

Waliser, D. E., Li, J. F., Woods, C. P., Austin, R. T., Bacmeister, J., Chern, J., et al. (2009). Cloud ice: A climate model challenge with signs and expectations of progress. *Journal of Geophysical Research*, *114*. http://doi.org/10.1029/2008JD010015

Wang, P.-H., McCormick, M. P., Poole, L. R., Chu, W. P., Yue, G. K., Kent, G. S., & Skeens, K. M. (1994). Tropical high cloud characteristics derived from SAGE II extinction measurements. *Atmospheric Research*, *34*(1–4), 53–83. http://doi.org/10.1016/0169-8095(94)90081-7

Wang, T., & Dessler, A. E. (2012). Analysis of cirrus in the tropical tropopause layer from CALIPSO and MLS data: A water perspective. *Journal of Geophysical Research-Atmospheres*, *117*(D4). http://doi.org/10.1029/2011JD016442

Wilson, D., & Ballard, S. (1999). A microphysically based precipitation scheme for the UK Meteorological Office Unified Model. *Quarterly Journal of the Royal Meteorological Society*, *125*(557), 1607–1636. http://doi.org/10.1002/qj.49712555707

Winker, D. M., Hostetler, C., Vaughan, M., & Omar, A. (2006). CALIOP algorithm theoretical basis document, Part 1: CALIOP Instrument and Algorithm Overview., 1–29.

Winker, D. M., Hunt, W. H., & Mcgill, M. J. (2007). Initial performance assessment of CALIOP. *Geophysical Research Letters*, *34*, L19803. http://doi.org/10.1029/2007GL030135

Winker, D. M., Pelon, J., Coakley, J. A., Ackerman, S. A., Charlson, R. J., Colarco, P. R., et al. (2010). The CALIPSO mission: A global 3D view of aerosols and clouds. *Bulletin of the American Meteorological Society*, *91*(9), 1211–1230. http://doi.org/10.1175/2010BAMS3009.1

Winker, D. M., Pelon, J., & Mccormick, M. P. (2003). The CALIPSO mission: Spaceborne lidar for observation of aerosols and clouds. In U. N. Singh, T. Itabe, & Z. Liu (Eds.), *Lidar Remote Sensing for Industry and Environment Monitoring III* (Vol. 4893, pp. 1–11). International Society for OpticalEngineering (SPIE Proceedings).

Winker, D. M., Vaughan, M. A., Omar, A., Hu, Y., Powell, K. A., Liu, Z., et al. (2009). Overview of the CALIPSO mission and CALIOP data processing algorithms. *Journal of Atmospheric and Oceanic Technology*, *26*(11), 2310–2323. http://doi.org/10.1175/2009JTECHA1281.1

Woods, S., Lawson, R. P., Jensen, E., Bui, T. P., Thornberry, T., Rollins, A., et al. (2018). Microphysical properties of tropical tropopause layer cirrus. *Journal of Geophysical Research: Atmospheres*, *123*(11), 6053–6069. http://doi.org/10.1029/2017JD028068

Yamashita, A. (1973). On the trigonal growth of ice crystals. *Journal of the Meteorological Scoiety of Japan*, *51*(5), 307–317. http://doi.org/10.2151/jmsj1965.51.5_307

Yang, Q., Fu, Q., & Hu, Y. (2010). Radiative impacts of clouds in the tropical tropopause layer. *Journal of Geophysical Research*, *115*. http://doi.org/10.1029/2009JD012393